Mismatch repair disturbs meiotic class I crossover control

Tim J. Cooper[1], Margaret R. Crawford[1], Laura J. Hunt[1], Marie-Claude Marsolier-Kergoat[2], Bertrand Llorente[3] and *Matthew J. Neale[1].

1. *Genome Damage and Stability Centre, School of Life Sciences, University of Sussex, UK*

2. CEA/DRF, I2BC/UMR 9198, SBIGeM, Gif-sur-Yvette, France; *CNRS-UMR 7026, Éco-anthropologie et Ethnobiologie, Musée de l'Homme, 17, Place du Trocadéro et du 11 Novembre, Paris, France.*

3. *Cancer Research Centre of Marseille, CNRS UMR7258, INSERM U1068, Institut Paoli-Calmettes, Aix-Marseille Université UM105, Marseille, France.*

Summary

Sequence divergence, mediated by the anti-recombinogenic activity of mismatch repair (MMR), forms a barrier to meiotic recombination and in turn the formation of viable gametes. However, rather than MMR acting as a non-specific impediment to meiotic recombination, here we provide evidence that at regions of greater sequence divergence MMR preferentially suppresses interfering (class I) crossovers (COs). Specifically, as measured in two *Saccharomyces cerevisiae* hybrids containing thousands of DNA-sequence polymorphisms, removal of MMR components increases both the frequency of CO formation and the uniformity of the observed CO distribution. At fine scale, CO positions are skewed away from polymorphic regions in MMR-proficient cells, but, critically, not when members of the class I CO pathway, *MSH4* or *ZIP3*, are inactivated. These findings suggest that class I COs are more sensitive to heteroduplex DNA arising during recombination. Simulations and analysis of Zip3 foci on meiotic chromosomes support roles for Msh2 both early and late in the class I CO maturation process. Collectively, our observations highlight an unexpected interaction between DNA sequence divergence, MMR, and meiotic class I CO control, thereby intimately linking the regulation of CO numbers and their distribution to pathways contributing to reproductive isolation and eventual speciation.

Introduction

Meiosis, a specialised two-step nuclear division, is responsible for the generation of genetically diverse, haploid gametes. An integral feature of the meiotic program is the initiation of homologous recombination via programmed Spo11-dependent DNA double-strand break (DSB) formation (Lam and Keeney, 2015). Subsequent steps of DSB repair leads to the formation of reciprocal, interhomologue exchanges known as

crossovers (COs)—visualised cytologically as chiasmata—that are essential for faithful disjunction of meiotic chromosomes during anaphase I (Gray and Cohen, 2016; Berchowitz and Copenhaver, 2010). Failure to form at least one CO per homologue pair risks the formation of aneuploid gametes, and thus the process of CO formation is highly regulated (Shinohara et al., 2008; Martini et al., 2006). Importantly, many DSBs—in some organisms the bulk of recombination events—repair without reciprocal exchange and are termed non-crossovers (Storlazzi et al., 1995; Baudat and de Massy, 2007a; Li et al., 2019).

Within many organisms, including *Saccharomyces cerevisiae* (the subject of this study), *Mus musculus*, *Homo sapiens* and *Arabidopsis thaliana*, two subclasses of CO co-exist. ZMM (Zip2-Zip3-Zip4-Spo16, Mlh1-Mlh3, Msh4-Msh5, Mer3)-dependent class I COs account for the majority of COs formed (~70-85% within *S. cerevisiae* (Lynn et al., 2007; de los Santos et al., 2003)). Class I COs are distributed more evenly along each chromosome than expected by chance via a process referred to as CO interference in which the formation of COs in proximity to one another appears suppressed (Berchowitz and Copenhaver, 2010). Class I CO formation requires the nuclease activity of Mlh1-Mlh3, a heterodimer otherwise involved in MMR (Zakharyevich et al., 2012; Cannavo et al., 2020; Kulkarni et al., 2020; Pannafino and Alani, 2021). The less abundant class II COs are non-interfering and depend upon the Mus81-Mms4, Yen1, or Slx1-Slx4 structure-specific nucleases (Holloway et al., 2008; de los Santos et al., 2003; Matos et al., 2011; Sarbajna et al., 2014).

Current models of class I CO formation suggest at least a two-step process involving, initially, the designation of a subset of precursor DSB intermediates by pro-class I CO factors (Bishop and Zickler, 2004). Although CO interference is proposed to become active at this stage, thereby shaping the distribution of COs along chromosomes, the final distribution of class I events is secondarily impacted by a later process: class I CO maturation (Zhang et al., 2014a). Rates of maturation less than 100% will specifically deplete class I COs. Such depletion can lead to achiasmatic chromosomes, or chromosomes with a residual CO positioned close to one or other telomere, where they are considered an “at-risk” location for successful segregation (Wang et al., 2017). Such ideas have been developed to help explain the relatively high rate of meiotic chromosome missegregation in human females relative to males (Wang et al., 2017).

Homologous recombination, the process responsible for both CO and NCO formation, requires a repair template with near-perfect sequence identity (Harfe and Jinks-Robertson, 2000). Mechanistically, Msh2, an essential MMR protein and orthologue of bacterial MutS (Reenan and Kolodner, 1992), is key in binding mismatches to promote their repair through the endonucleolytic action of the Mlh1-Pms1 and Mlh1-Mlh3

complexes (Kolodner and Marsischky, 1999; Srivatsan et al., 2014). Such mismatch detection by Msh2 is thereby integral to preventing recombination by mechanisms that include recruitment of the anti-recombination helicase Sgs1 to heteroduplex DNA (Goldfarb and Alani, 2005). As such, in MMR-proficient *S. cerevisiae* hybrids, recombination between polymorphic homoeologous substrates is inefficient, leading to reduced rates of meiotic CO formation, reduced spore viability, and increased chromosomal non-disjunction during meiosis I (Chambers et al., 1996; Hunter et al., 1996)—phenotypes linked to incipient speciation, and which are largely reversed within MMR-deficient strains (Greig et al., 2003; Hunter et al., 1996; Martini et al., 2011; Chambers et al., 1996; Spies and Fishel, 2015; Bozdag et al., 2021). However, whilst Msh2-dependent binding to mismatches it likely to be rapid (Zhai and Hingorani, 2010), the precise stage of the HR pathway(s) that mismatch recognition arises, and whether this is the same for all intermediates, and in all organisms, is unclear. Indeed, recent observations in mouse meiosis suggest only limited impact of MMR activity on recombination suppression (Peterson et al., 2020), and perhaps more intriguingly, observations in *Arabidopsis thaliana* indicate an unexpected association (rather that inhibition) of recombination within polymorphic regions (Blackwell et al., 2020). Given the fundamental intimate relationships between MMR, sequence divergence, and meiotic recombination, such observations highlight the need to thoroughly explore, and to understand better, the impacts that meiotic MMR activity may have across biology.

Results

Deletion of *MSH2* alters the genome-wide frequency and distribution of meiotic crossovers

In order to investigate the impact sequence divergence and the process of mismatch repair has upon meiotic CO formation in the budding yeast, *S. cerevisiae*, we mapped recombination patterns genome-wide (**Fig. 1a** and **Methods**) within six wild-type and thirteen MMR-defective *msh2*Δ meioses—obtained from a hybrid of two widely utilized laboratory isolates: S288c and SK1 (~65,000 SNPs, ~4,000 high confidence INDELs, ~0.57% divergence; (Martini et al., 2011; Marsolier-Kergoat et al., 2018)). Additionally, we reanalyzed datasets comprising fifty-one wild-type (Mancera et al., 2011; Chen et al., 2008) and four *msh2*Δ (Oke et al., 2014) tetrads from a S96 x YJM789 hybrid of *S. cerevisiae* (~0.6% divergence). On average, we identified 74.3 ±5.4 and 105.9 ±7.8 COs per meiosis within our SK1 x S288c wild-type and *msh2*Δ samples respectively, corresponding to a significant 1.4-fold increase in CO frequency ($p<0.01$; Two-sample T-test) (**Fig. 1b** and **Supplementary Table 1**). A significant *msh2*Δ-dependent increase (~1.25-fold, $p<0.01$; Two-sample T-test) was also observed within the S96 x YJM789 hybrid (**Fig. 1b** and **Supplementary Table 1**)—collectively reaffirming the known anti-recombinogenic activity of Msh2. Notably, CO frequencies were considerably higher

within S96 x YJM789 than S288c x SK1 (91.4 vs. 74.3 COs per wild type meiosis)—suggesting that cross-specific differences may exist.

Deletion of *MSH2* also increased observed NCO events in both hybrid crosses (SK1 x S288c: wild type = 30.8; *msh2*Δ = 92.8; S96 x YJM789: wild type = 46.8; *msh2*Δ = 56.3; **Supplementary Table 1**), supporting the established effect of Msh2 in suppressing both COs and NCOs in hybrid strains as reported previously (Martini et al., 2011). However, unlike COs, the visibility of NCOs is directly affected both by the true number of converted and/or heteroduplex markers contained within a NCO event, and by the technical efficiency of calling what may potentially be only short regions of contiguous nonreciprocal marker change (Marsolier-Kergoat et al., 2018; Ahuja et al., 2021). NCO frequencies are also more affected by homeostatic effects than are COs (Martini et al., 2006). For these reasons, quantitative comparisons of NCO frequency changes in the presence and absence of *MSH2* are not simple to interpret. Instead, we focused our attention on COs where event visibility is assumed to be similar in the presence and absence of Msh2.

To investigate any possible effect of Msh2 on CO patterning, we determined the distribution of inter-crossover distances (ICDs)—the separation (in bp) between successive COs along every chromosome. To accommodate comparisons between different sample sizes, ICDs were transformed (**Methods** and **Supplementary Fig. 1**) and visualized in rank order as empirical cumulative distribution functions (eCDFs). In all mapped strains, CO distributions deviated significantly ($p<0.01$; Two-sample Kolmogorov-Smirnov (KS) test (Massey Jr, 1951)) from simulated conditions in which the same frequency of observed COs were distributed randomly relative to one another (**Fig. 1c–f**). In particular, observed patterns displayed a more homogenous distribution of ICDs, with fewer short and long distances between adjacent COs than expected by chance. This change in distribution was visible as a steeper eCDF curve in the experimental data compared to the random simulation, a feature that was stronger within the S96 x YJM789 cross (**Fig. 1d**) than within S288c x SK1 (**Fig. 1c**), additionally suggesting that the meiotic CO landscape is regulated in a cross-specific manner (**Supplementary Fig. 2** and **Extended discussion**).

Unexpectedly, deletion of *MSH2* within both hybrid crosses caused ICD curves to skew yet further away from the random simulation, creating a steeper inflection point (**Fig. 1c-d**; $p < 0.01$; Two-sample KS test) indicative of increased homogeneity in the spacing of COs relative to one another. Removal of a second MMR factor, *PMS1*, which acts downstream of Msh2 mismatch binding (Prolla et al., 1994), caused similar changes to both the CO frequency and the CO distribution curves relative to wild type (**Supplementary Fig. 3a-b**), but no

additive effect in a double *msh2*Δ *pms1*Δ strain was observed—thereby suggesting that these CO changes arise as a general consequence of MMR inactivation.

To account for any impact increased CO frequency may have upon CO distribution, we utilized an *ndt80AR* ("arrest–release") strain where meiotic prophase length is extended via temporary repression of the Ndt80 transcription factor (Benjamin et al., 2003; Xu et al., 1995; Crawford et al., 2018). On average, we identified 94.5 ±16.3 COs per meiosis within *ndt80AR*—a significant increase relative to wild type ($p<0.01$; Two-sample T-test) (**Fig. 1b**). However, no further increase occurred upon deletion of *MSH2* (*msh2*Δ *ndt80AR*, 97.5 ±15.4 COs, $p=0.87$; Two-sample T-test) (**Fig. 1b**). Importantly, despite the lack of change in CO frequency, the *msh2*Δ-dependent skew in CO distribution was still observed in *ndt80AR msh2*Δ (**Fig. 1e**) whereas increased CO frequency alone (*ndt80AR*) did not alter CO distribution compared to wild type (**Fig. 1f**) ($p=0.91$; Two-sample KS test).

Inactivation of MMR within hybrid *S. cerevisiae* strains therefore gives rise to two distinct phenotypes relative to wild type: (i) increased CO frequency, as previously observed (Martini et al., 2011), and (ii) a global shift in the distribution of COs relative to one another—something that can arise independently of changes in CO frequency. Whilst we are not directly measuring interference between COs by these analyses, the latter change to the CO distribution is consistent with the loss of MMR activity appearing to increase the presence and/or impact of CO interference within the global pool of COs.

Mixture modelling of class I and class II CO distributions

CO distributions can be modelled by the gamma (γ) distribution, where γ(α) values >1.0 indicate increasing deviations from randomness (potentially indicating increasing strength of interference between COs) (McPeek and Speed, 1995). Importantly, however, because the experimentally observed CO distribution is a composite mixture of class I (interfering) and class II (non-interfering) COs, models based on a single (γ) distribution deviate substantially from experimental data, which contains many more ICDs <50 kb than expected (**Fig. 2a**). Indeed, the presence of these short ICDs is consistent with the presence of the subpopulation of randomly distributed COs (i.e. class II).

To explore this aspect of the data, we utilised a computational method based on (γ)-mixture modelling (**Fig. 2b**), to statistically deconvolute ICD data, thereby deriving estimates of the random and non-random components (**Methods**). A similar approach has been developed by others to explore the parameters

governing the physical positioning of COs along chromosomes (Gauthier et al., 2011). A non-random ($\gamma(\alpha_I)$ >3.0), and a random ($\gamma(\alpha_{II})$ ~1.0) component was identified for all genotypes (**Fig. 2d**). Composite simulations (**Supplementary Fig. 4**) using the estimated proportions of these two CO distributions improved model fit to experimental data and eliminated the deviations between simulation and experimental data otherwise observed for ICDs below 50 kb (**Fig. 2c**). We henceforth refer to these random and non-random CO components as estimates of, respectively, the class II and class I CO components.

Consistent with prior estimates (de los Santos et al., 2003), using this analysis, *MSH2* wild type class I:class II ratios were estimated at ~2.0 and ~3.0 within S288c x SK1 and S96 x YJM789 respectively (**Fig. 2d**). By contrast, deletion of *MSH2* increased ratio estimates to ~5-6 in both hybrid crosses (**Fig. 2d**), suggesting a ~1.7-fold increase in class I CO formation in the absence of Msh2 (**Fig. 2e**). These models also estimated *msh2*Δ-dependent decreases in the absolute frequency of class II CO formation (~0.5 to 0.7-fold) (**Fig. 2f**). Importantly, the $\gamma(\alpha_I)$ value estimates obtained for the non-random (class I) CO population were broadly similar for all strains, irrespective of Msh2 status or estimate of total class I CO frequency (gamma values between ~3.0–3.8; **Fig. 2d**, Mixed fit)—and different from the poorly fitting global $\gamma(\alpha_s)$ estimates (1.43–2.44) generated from fitting a single gamma distribution to each entire dataset (**Fig. 2d**, Single fit).

Thus, assuming that our modelling of a mixed gamma distribution is a reasonable estimate of the class I : class II balance present within cells, these analyses suggest that the global change in CO distribution towards less randomness in *msh2*Δ arises not from an increase in CO interference strength between class I COs, but instead from a change in the relative proportion of class I and class II COs present within the total CO pool. Specifically, our results suggest that the formation of ZMM-dependent class I COs is preferentially favoured within Msh2-deficient cells and that most of the additional COs observed within *msh2*Δ relative to wild type are class I. Put another way, our observations suggest that the activity of Msh2 disproportionately impedes the formation of class I COs relative to class II.

Distribution and frequency of Zip3 foci appear unaltered in *msh2*Δ

Zip3 foci specifically mark the sites of interfering, class I COs (Agarwal and Roeder, 2000; Zhang et al., 2014b). Our computational analysis predicts an increase in Zip3-marked CO sites, but no change in their relative distribution along synapsed chromosome axes. Thus, to investigate the results of our modelling, we counted Zip3 foci (Shinohara et al., 2008) on spread meiotic chromosome preparations from S288c x SK1 hybrids co-labelled with Zip1-GFP (White et al., 2004), an established marker of chromosome synapsis in *S. cerevisiae*

192 (**Fig. 3a-b** and **Supplementary Fig 5**) (Henderson and Keeney, 2004). To reduce observational bias, samples
193 were randomised, and counting was restricted to only well-spread nuclei showing clear thread-like patterns of
194 Zip1. Overall, focus number per nucleus was highly variable (10–50 per cell). Perhaps because of this
195 variation, we were unable to identify any reproducible differences in foci number upon *MSH2* deletion, both in
196 the wild-type and the pachytene-arrested *ndt80AR* strain background. However, we cannot exclude that this
197 high variance obscures a real difference.
198
199 Within these data we noticed a modest correlation between spread size and total foci count per spread
200 (**Supplementary Fig. 6a**). Thus, to investigate whether technical differences in spreading efficiency was
201 affecting Zip3 foci counts we further analysed the density of Zip3 foci per μm^2 of spread area bounded by the
202 chromosomal (DAPI) signal, but, again, found no clear differences caused by *MSH2* deletion (**Supplementary**
203 **Fig. 6b**).
204
205 We next analysed the relative distribution of Zip3 foci along synapsed chromosome axes—a potential indicator
206 of CO interference—in cells arrested at the pachytene stage via the *ndt80AR* allele (**Fig. 3c-f**). Measuring the
207 distances between Zip3 foci along the subset of well-resolved chromosomes in each strain demonstrated
208 significant deviation from that expected for a random distribution (**Fig. 3e**) and instead much closer to that of
209 a simulated interfering distribution (**Fig 3f**), as expected for Zip3 foci marking interfering Class I events (Zhang
210 et al., 2014b). However, no additional distributional differences were detected in the absence of Msh2 (**Fig.**
211 **3e-f**). The similarity of the Zip3 foci distribution in the presence and absence of Msh2 is consistent with our
212 mixture-modelling analysis of CO positions identified in the genome-wide data, which estimated a similar $\gamma(\alpha_I)$
213 parameter for the non-random component in all strains regardless of *MSH2* status (**Fig 2d**, above).
214
215 Whilst the large variation in Zip3 foci frequencies limits our ability to draw firm conclusions, taken together, our
216 observations suggest that the differences in CO frequency and patterning that are observed in our genome-
217 wide analysis with and without *MSH2* may arise downstream of the point at which we have assessed Zip3 foci
218 counts ("pachytene" as mediated by *ndt80*Δ arrest). Specifically, changes in the efficiency of CO designation
219 and/or maturation arising after this arrest point, and/or independent of Zip3 focus formation, could lead to
220 differences in observed (Zip3 foci) and final (genome-wide analysis in tetrads) CO frequency and distribution.
221 This possibility is explored in more detail below.
222
223

Msh2 specifically impedes class I CO formation at regions of greater sequence divergence

The MMR machinery forms a potent barrier to homoeologous recombination, presumably due to recognition and destabilisation of recombination intermediates containing DNA mismatches. To directly explore the interplay between DNA mismatches and CO formation, we calculated polymorphism densities (SNPs, Indels) ±500 bp around every mapped CO (**Fig. 4a**) and compared between genotypes. To generate a comparative reference point, the expected environment for meiotic recombination, as defined by the polymorphism density surrounding ~3600 DSB hotspot midpoints (Pan et al., 2011), was also calculated. Polymorphism density surrounding COs within *MSH2* wild-type strains (S288c x SK1: wild type, *ndt80AR*) was significantly different to that expected in both distribution ($p<0.01$; Two-sample KS test) and in mean variant density (5.32 vs. 6.18, $p<0.01$; Two-sample T-test)—characterized by a skew towards COs, on average, arising within regions of lower genetic divergence than expected from the genome-wide position of DSBs (**Fig. 4b**). By contrast, the polymorphism density around *msh2*Δ COs displayed visual and statistical similarity to that expected ($p>0.25$; Two-sample KS-test) (6.26 vs. 6.18, $p = 0.52$; Two-sample T-test) (**Fig. 4b**). Such a disparity between wild type and *msh2*Δ was recaptured within the independent S96 x YJM789 hybrid where COs were again skewed towards regions of lower polymorphism density only in the *MSH2* wild-type strain (**Fig. 4c**). A similar effect was observed when considering polymorphism density arising ±1000 bp around each CO but was diminished with increasing distance (±2000 bp)—suggesting that DNA mismatches exert a localised inhibitory effect on CO formation (**Supplementary Fig. 7a-b** and **Supplementary Discussion**).

Our mixture modelling suggests that inactivation of *MSH2* alters global CO distribution by altering the relative abundance of class I vs class II COs (**Fig. 2** and **Fig. 3**). To determine whether the influence that Msh2 has in regulating CO class outcome is related to its role in suppressing COs at sites where mismatches will arise during meiotic recombination, we further calculated polymorphism densities within mutants that disrupt class I (*zip3*Δ, *msh4*Δ) or class II (*mms4*Δ) CO formation (Oke et al., 2014). Strikingly, mutants devoid of class I COs phenocopied *msh2*Δ—that is, COs within these mutants were no longer skewed away from regions of higher polymorphism density despite the presence of Msh2—sharing mean polymorphism densities around COs that were not statistically dissimilar to expected ($p>0.5$; Two-sample T-test) (**Fig. 4b-c**). Moreover, the impact of *zip3*Δ and *msh2*Δ appeared to be epistatic rather than additive, with no further change in the double mutant (**Fig. 4b**), suggesting a single common pathway. By contrast, removal of class II formation (*mms4*Δ) had no impact on the interplay between CO formation and polymorphism density (**Fig. 4c**)—collectively suggesting that mismatch-dependent repression of CO formation is specific to class I COs.

256 **Msh2 activity during class I CO maturation**

257 Whilst our observations provide strong evidence to support a disproportionate impact of Msh2 and
258 polymorphisms on COs formed via the class I pathway, the time and mode of action within the HR process
259 that this occurs is unclear. To explore in more detail the possibility of early (designation) versus late
260 (maturation) action of Msh2, we generated simulations in which mixed patterns of COs (ranging from 100%
261 class I to 50% class I : 50% class II) were subject to varying rates of stochastic class I CO failure (up to 50%
262 loss)—simplistically mimicking the possible outcome of class I CO maturation failure at a (late) stage
263 downstream of interference-patterned CO designation (**Fig. 5a** and **Methods**). Resulting genome-wide
264 patterns of simulated CO formation (presented as eCDF curves of inter-CO distances as in **Fig. 1c-f**) were
265 then compared to our experimentally observed CO patterns and tested for statistical similarity (**Fig. 5b-g**). For
266 *msh2*Δ datasets, in both SK1xS288c (**Fig. 5b-c**) and S96xYJM (**Fig. 5d**), better fits (P>0.9, KS test) were
267 obtained only for parameter combinations in which either class II CO formation was low (as described above)
268 and/or maturation failure was low—consistent with the relatively regular (interfering) genome-wide pattern of
269 COs observed in these strains (**Fig. 1c-f**).

270

271 By contrast, and as described above, wild-type cells, where Msh2 is active, displayed global CO patterns that
272 were better fit (P >0.9; KS Test) with a greater proportion of class II COs (**Fig. 5e-g**; ~30% in SK1xS288c;
273 ~20% in S96xYJM). However, these simulations also identified a diagonal band of reasonable parameter fits
274 (P >0.8; KS Test) where decreasing proportions of class II COs were offset by increasing chances of class I
275 CO maturation failure (**Fig. 5e-g**). This trend was clear, albeit relatively modest, in the SK1xS288c hybrid, but
276 was enhanced in S96xYJM, where the highest density of good statistical fits (P>0.9; KS test) was obtained for
277 relatively low fractions of class II COs (~5-10%), similar to the estimates obtained in *msh2*Δ cells, but with high
278 rates of class I CO maturation failure layered on top (20-40%; **Fig. 5g**).

279

280 Collectively, our simulations suggest that intrinsic rates of class I maturation failure may be quite low in *msh2*Δ
281 hybrid cells. By contrast, mismatch-dependent class I maturation failure, downstream of CO designation, and
282 thus potentially quite late in meiotic prophase, may underpin at least some of the apparent reductions in class
283 I COs observed in *MSH2* control cells—an effect that may be more prevalent in certain hybrids such as
284 S96xYJM.

285

286

287

Discussion

Sequence divergence suppresses recombination within a wide range of eukaryotes including *S. cerevisiae*, *M. musculus* and *H. sapiens* (Chambers et al., 1996; Hunter et al., 1996; Bozdag et al., 2021; Cole et al., 2010; Baudat and de Massy, 2007b; Jeffreys and Neumann, 2005). Findings presented here expand upon these observations and suggest that the anti-recombinogenic activity of Msh2, exerted at homoeologous sites, does not mediate an indiscriminate suppression of COs but rather acts disproportionately at sites of ZMM-dependent, interfering COs (**Fig. 6a-c**)—thereby altering the spatial distribution of CO recombination across the genome by modulating the class I : class II balance. Our observations underscore how even the low rates of divergence (~0.6%) present within intra-specific hybrids of *S. cerevisiae* can generate global changes in CO frequency, CO type, and genome-wide distribution. Nevertheless, in wild-type hybrids when Msh2 is active, COs still frequently arise within heterologous regions (**Fig. 4b-c**) with class I COs still forming at a high rate (67%-75% of total COs; **Fig. 2d**). Mismatches do not, therefore, form an absolute barrier to class I COs, but instead seem to influence the probability of their formation.

Current models posit that the establishment and differentiation of class I COs is a multi-step process starting with nascent recombination interactions initiated by Spo11 DSBs, designation as class I precursors, and subsequent maturation into the final class I COs (Zhang et al., 2014a). Inefficient maturation—downstream of the implementation and patterning effects of CO interference—has been proposed as a mechanism to explain CO patterns and the innate predisposition towards meiotic chromosome missegregation in human females (Wang et al., 2017).

Within this framework, it is therefore important to consider at what stage Msh2 activity causes class I CO precursors to be redirected towards alternative outcomes. Prior analyses aimed at elucidating the CO differentiation process have harnessed relatively deep (rather than broad) datasets in order to build probability distributions of expected coincident class I COs at adjacent positions along specific chromosomes (Zhang et al., 2014a). By contrast, our genome-wide maps of CO position are broad, encompassing positional information for every CO on every chromosome in individual meioses, but are of limited depth at any given locus due to the limited throughput of genome-wide sequencing of meiotic progeny (six wild type and thirteen *msh2*Δ meioses in the S288c x SK1 hybrid). These differences preclude us from performing a similar analysis. Moreover, unlike the specificity of Zip3-focus analysis for class I COs, genome-wide CO maps cannot yet distinguish between class I and class II COs at any given site. For these reasons, we have focused on

319 analysing Msh2-dependent differences in the fine-scale positions of COs and in the distribution of COs relative
320 to one another.
321
322 When considering global CO positions, conversion from a class I to a class II CO would still give rise to a CO
323 in the same position and with no change in global CO frequency. Thus, because we observe changes in CO
324 pattern and frequency, we infer that most Msh2-redirected class I events become NCOs and/or become
325 otherwise invisible within our assay (**Fig. 6c**). On this latter point, recent work provides evidence for frequent
326 repair-template switches between homologues and sister chromatids (Marsolier-Kergoat et al., 2018; Ahuja et
327 al., 2021), and thus redirection of CO precursors towards repair exclusively using identical sequences on the
328 sister chromatid is also possible (events that would be invisible in our assays). However, such redirection
329 would seemingly need to happen prior to the priming of DNA synthesis by a DSB end that has invaded the
330 homologue (**Fig. 6a**). Alternatively, Msh2-dependent redirection towards inter-sister events and NCOs may
331 occur concomitantly with mismatch repair, leading in some cases to restoration of any heteroduplex markers
332 back to the parental configuration, again precluding detection by our methods (**Fig. 6c**).
333
334 The fact that the estimated frequency of class II COs was greater, in absolute terms, in Msh2-proficient cells
335 suggests that Msh2-dependent suppression of class I COs may indirectly influence class II CO formation. For
336 example, more class II events (arising from increased Spo11 activity) might be enabled by spatial and/or
337 temporal changes in the efficiency of homologue engagement caused by MMR-dependent rejection of nascent
338 recombination events, similar to when class I CO formation (Thacker et al., 2014) and/or chromosome synapsis
339 (Mu et al., 2020) is disturbed by genetic mutation. However, we did not detect any obvious Msh2-dependent
340 differences in synapsis within hybrid strains (**Fig. 3b**), suggesting that, if present, such effects are transient
341 and/or relatively subtle.
342
343 In our envisioned model (**Fig. 6a-c**), which builds upon prior ideas (Chambers et al., 1996; Hunter et al., 1996),
344 rejected class I events may be redirected towards the NCO pathway relatively early on during CO designation
345 and/or maturation via unwinding of the initial strand invasion intermediate with repair proceeding via synthesis-
346 dependent strand annealing (SDSA; (Marsolier-Kergoat et al., 2018; Ahuja et al., 2021)). Alternatively,
347 redirection could occur at a later stage, for example after class I CO precursors reach the double Holliday
348 junction (dHJ) stage. The potential for dHJs to undergo branch migration (Marsolier-Kergoat et al., 2018; Ahuja
349 et al., 2021) may generate large patches of heteroduplex DNA that could in turn be efficiently detected by the
350 MMR machinery and stimulate Sgs1-Top3-Rmi1-dependent dissolution. It is also possible that mismatches

351 cause dHJs to be more-frequently resolved as NCOs nucleolytically (perhaps via nicks generated by the MMR
352 process itself), whereas an almost absolute bias towards CO resolution is observed in the absence of Msh2
353 (Marsolier-Kergoat et al., 2018).
354
355 Our apparent inability to detect Msh2-dependent differences in the frequency of Zip3-marked CO precursors
356 at the pachytene-like arrest enforced by *NDT80* deletion where dHJs accumulate (**Fig. 3**; (Allers and Lichten,
357 2001)), indeed suggests that at least some class I redirection may arise after this dHJ stage. A late-stage
358 activity of Msh2 that disturbs class I CO formation would also be compatible with our simulations of CO
359 maturation failure in wild-type, but not *msh2*Δ cells (**Fig. 5**). However, why the two hybrids studied here
360 behaved differently in this regard is unclear but might suggest differing propensity for Msh2 to elicit anti-CO
361 effects before, during, or after CO patterning has completed.
362
363 It is also possible that the distributional differences in CO patterns we have observed are patterned by
364 processes that are independent of CO interference and the class I or class II CO pathways. Non-uniform
365 densities of DNA-sequence polymorphisms, DSBs, and even COs themselves all have the potential to
366 influence the relative CO distributions that arise on a per-cell basis. However, polymorphisms, DSBs, and COs
367 are relatively evenly spread across the entire length of each chromosome in *S. cerevisiae* (**Supplementary**
368 **Fig. 8a-d**), and thus as expected, biasing CO site selection by these underlying population-level parameters
369 had no measurable impact on resulting patterns of simulated inter-CO distributions (**Supplementary Fig. 8e-**
370 **g**). Nevertheless, we recognise that non-random distributions of precursor events in individual cells can
371 influence downstream patterns of COs (Zhang et al., 2014a), without necessarily generating nonuniformity
372 when assayed across a population. In addition, in organisms with less uniform SNP/indel density, and/or
373 propensity to initiate recombination, such non-uniformity could result in a redistribution of CO formation towards
374 certain regions, potentially influencing relative CO patterning on a per-cell basis (e.g. the effect that highly
375 heterologous regions have in *A. thaliana* (Ziolkowski et al., 2015)).
376
377 In mitotic cells, inhibition of homoeologous recombination by means of heteroduplex rejection, relies upon
378 Msh2 and the RecQ-family helicase, Sgs1 (Sugawara et al., 2004; Goldfarb and Alani, 2005; Spies and Fishel,
379 2015). An *sgs1*Δ mutant may therefore be expected to phenocopy *msh2*Δ if suppression of class I COs occurs
380 via this mechanism. Intriguingly, however, the distribution of COs is more random in *sgs1*Δ relative to wild type
381 (**Supplementary Fig. 3c**), suggesting a decrease in the proportion of class I COs. Moreover, *sgs1*Δ also
382 abolishes the increased skew towards nonrandomness (inferred above to indicate an increased frequency of

class I COs) caused by *MSH2* deletion (**Supplementary Fig. 3d**)—suggesting that Msh2 and Sgs1 are not epistatic, but rather antagonistic in the formation of class I COs. Thus, it is possible that Msh2 mediates suppression of class I COs in a pathway different to that of Sgs1-mediated heteroduplex rejection, instead relying upon the downstream properties or factors of MMR, including Pms1 (**Supplementary Fig. 3a**), to achieve its effect. Alternatively, the genetic complexity outlined above may arise because Sgs1 can act at multiple steps and on a range of recombination intermediates. For example, at early stages Sgs1 could act to promote class I CO formation by unwinding nascent recombination intermediates—independently of Msh2 and mismatches—thereby allowing them to be recycled into future potential class I precursors (Oh et al., 2007; Tang et al., 2015; Kaur et al., 2015). By contrast, perhaps mediated by mismatch- and Msh2-dependent destabilisation of pro-class I CO factors, Sgs1 activity at a later stage could promote dHJ dissolution thereby suppressing class I maturation.

It is important to consider how MMR-specificity for class I COs may arise. Msh2, Mlh1 and Pms1 form a ternary complex during MMR (Li, 2008) and *in vitro* data suggest that Mlh1-Mlh3—essential class I CO factors—facilitate binding of Msh2 to heteroduplex DNA arising, for example, at sites where mismatches exist between parental strains (Rogacheva et al., 2014). Msh2 itself, via interaction with Msh6, also directly binds Holliday junctions with high affinity (Alani et al., 1997). Thus, Mlh1-Mlh3, or the inherent structure of class I precursors, may be responsible for the differential sensitivity of each CO subclass to sequence mismatches through preferential recruitment or activation of Msh2 and MMR at class I sites. Indeed, available data (Getz et al., 2008) suggest that Class I COs are more likely to recruit MMR and lead to conversion/restoration (6:2, 4:4 patterns)—or possibly rejection (our results). By contrast, class II COs are less likely to recruit MMR, and thus not only survive in MMR-proficient cells but also show signs of post-meiotic segregation (Getz et al., 2008). Such mechanisms would fit with the specific reductions in class I COs that we observe in MMR-proficient cells.

Given the evolutionary conservation of MMR and of the fundamental process of CO recombination in meiosis, an important consideration is whether the processes uncovered by our study are conserved across biology. With this in mind, it is interesting to note that a detailed analysis of two Spo11-DSB hotspots in *M. musculus* found no evidence for MSH2-dependent suppression of recombination (Peterson et al., 2020). Furthermore, a recent genome-wide study in *A. thaliana* indicates redistribution of COs towards, rather than away from, polymorphic regions in MMR-proficient control lines relative to a *msh2* mutant (Blackwell et al., 2020). Thus, it will be critical to elucidate what are the mechanistic relationships that underpin these species-specific observations. Such differences may be directed by species-specific modulation of MMR activity at pro-CO

sites, or by fundamental genome-scale differences that influence meiotic recombination, such as chromosome size, global recombination rate (high in yeast), distribution of DNA sequence heterozygosity (non-uniform in *A. thaliana*), and regulation of recombination initiation (PRDM9 dependent in *M. musculus*).

Overall, understanding the molecular mechanisms that contribute to speciation is fundamental to our understanding of biological diversity and evolution. In this regard, despite many unknowns remaining, our observations highlight an unexpected link between DNA sequence divergence, MMR, and meiotic class I CO control, thereby intimately linking the regulation of CO numbers and their distribution to pathways contributing to reproductive isolation and eventual speciation.

Contributions

T.J.C, M.R.C. and M.J.N. conceived of the project. M.R.C. performed all wet-lab work, data processing and event calling associated with the genome-wide mapping. T.J.C. analysed and interpreted the data, performed in-silico simulations, and designed the modelling algorithms. L.J.H. performed all microscopy and foci analysis. M.M.K. and B.L. provided scripts, protocols, additional samples, and ideas. T.J.C., M.J.N., and B.L. wrote the manuscript with critical input from all authors.

Acknowledgements

We thank A. Shinohara for sharing anti-Zip3 antibody (Shinohara et al., 2008) and R. M. Allison for help with image acquisition.

Competing interests

The authors declare no competing financial interests.

Corresponding authors

Correspondence to:

Matthew J. Neale (m.neale@sussex.ac.uk) and Bertrand Llorente (bertrand.llorente@inserm.fr)

Funding

T.J.C, M.R.C, L.J.H and M.J.N were supported by an ERC Consolidator Grant (#311336), the BBSRC (#BB/M010279/1) and the Wellcome Trust (#200843/Z/16/Z).

446 B.L. lab was funded by the ANR-13-BSV6-0012-01 grant from the Agence Nationale de la Recherche and a
447 grant from the Fondation ARC pour la Recherche sur le Cancer (SFI20121205448).

448

449 Data Availability

450 Raw sequence data is deposited in the NIH Sequence Read Archive (SRA) under accession numbers
451 SRP151982 (wild type, *msh2*Δ, *ndt80AR*), SRP111430 (*msh2*Δ), and SRP152953 (*zip3*Δ). Scripts, tools,
452 software and additional data are available at: https://github.com/Neale-Lab and
453 https://github.com/NealeTools/RecombineSim

454

455 Methods

456 Yeast Strains

457 All Saccharomyces cerevisiae strains used in this study are derivatives of SK1 (Kane and Roth, 1974) and
458 S288c (Mortimer and Johnston, 1986). Hybrid strains, utilised in genome-wide mapping, were derived from a
459 cross of haploid SK1 and S288c, or used published datasets from a cross of S96 x YJM789 (Chen et al., 2008;
460 Mancera et al., 2008; Oke et al., 2014; Al-Sweel et al., 2017). Strain genotypes are detailed in (**Supplementary
461 Table 2**). Knockouts were performed and tested by standard transformation and PCR techniques (Longtine et
462 al., 1998). *msh2*Δ::*kanMX6* and *zip3*Δ::*HphMX* were generated by PCR mediated gene replacement using a
463 pFA6a-*kanMX6* or pFA6-*hphMX* plasmid (Goldstein and McCusker, 1999). The P_{GAL}-*NDT80::TRP1* allele has
464 the natural *NDT80* promoter replaced by the *GAL1-10* promoter, and strains include a *GAL4::ER* chimeric
465 transactivator for β-estradiol-induced expression (Benjamin et al., 2003). For cytological analyses in hybrid
466 strains, Zip1-GFP (White et al., 2004) was expressed heterozygously from the SK1 parent only. S288c x SK1
467 hybrids create viable spores (91.98% WT, 72.99% *msh2*Δ spore viability), limiting observational bias that may
468 arise from assaying a limited, surviving population (Crawford et al., 2018).

469

470 Meiotic Timecourse (*ndt80AR* strains)

471 Diploid strains were incubated at 30°C on YPD plates for 48h. For SK1 diploids, a single colony was inoculated
472 into 4 mL YPD (1% yeast extract, 2% peptone, 2% glucose) and incubated at 30°C at 250 rpm for 24 h. For
473 hybrid crosses, haploid parental isolates were mated in 1 mL YPD for 8 h. An additional 3 mL of YPD was
474 subsequently added and the cells were grown for 16 h. Cells were inoculated to a density of (OD600) 0.2 into
475 30 mL YPA (1% yeast extract, 2% peptone, 1% K-acetate) and incubated at 250 rpm at 30°C for 14h. Cells
476 were collected by centrifugation, washed in H_2O, and resuspended in 30mL pre-warmed sporulation media

477 (2% potassium acetate, 5 µg/mL Adenine, 5 µg/mL Arginine, 5 µg/mL Histidine, 15 µg/mL Leucine, 5 µg/mL
478 Tryptophan, 5 µg/mL Uracil). The culture was then incubated at 30°C at 250 rpm for the duration of the time
479 course. After 8h, 2 mL of the synchronised cultures were split and exposed to β-estradiol to a final
480 concentration of 2 mM, which induces the transcription of *NDT80* and thus sporulation. Cultures were then
481 incubated to a total of 48 h at 30°C prior to dissection. For microscopy cells were pre-grown in BYTA medium
482 (buffered 1% yeast extract, 2% tryptone, 1% K-acetate) and *ndt80AR* cultures were not released with β-
483 estradiol.
484

485 **Tetrad Dissection**

486 In order to produce hybrid spores for sequencing, SK1 x S288c haploid parents were mated for 8-14 h on YPD
487 plates, with the exception of *ndt80AR* strains, which were mated and grown in liquid YPD for 24 h (see above).
488 Haploids were mated freshly on each occasion and not propagated as diploids in order to reduce mitotic
489 recombination. Sporulation was induced, and tetrads were dissected after 72 h in 2% potassium acetate. For
490 octads, spores were additionally grown for 4–8 h on YPD plates until a single mitotic division had completed,
491 after which the mother-daughter pair were separated. Colonies were grown for 16 h within liquid YPD for
492 genomic DNA extraction. Only tetrads and octads producing four or eight viable spores/colonies, respectively,
493 were considered for genotyping by NGS.
494

495 **NGS Library Preparation**

496 Genomic DNA was purified from overnight, saturated YPD cultures using standard phenol-chloroform
497 extraction techniques. Samples of genomic DNA were diluted to 0.2–0.3 ng/µL. DNA concentration was
498 measured using the Qubit High Sensitivity dsDNA Assay. Genomic DNA was fragmented, indexed and
499 amplified via the Nextera XT DNA library Prep Kit according to the best practices recommended by Illumina.
500 In order to check fragment-length distribution and concentration of purified libraries, 1 µL of undiluted library
501 was run on an Agilent Technology 2100 Bioanalyzer using a High Sensitivity DNA chip. To pool samples for
502 sequencing, 5 µL of each sample was combined into a 1.5 mL tube and mixed. 24 µL of the mix was transferred
503 to a tube containing 570 µL hybridisation buffer. The mix was boiled at 96°C for 2 minutes and placed in ice
504 water for 5 minutes. 6 µL of denatured PhiX control (prepared according to Illumina protocol, final concentration
505 1%) was added to the library, mixed well and then loaded into a MiSeq reagent cartridge. Sequencing was
506 performed in-house using an Illumina MiSeq instrument.
507
508

509 **Alignment, SNP and indel Detection**

510 Individual spores were sequenced to an average read-depth of ~45x. Initially, paired-end read FASTQ files
511 are aligned, via Bowtie2 (Langmead and Salzberg, 2012), to the SacCer3 reference genome (v. R64-2-1;
512 (Engel and Cherry, 2013)) using the parameters: -X 1000 —local —mp 5,1 -D 20 -R 3 -N 1 -L 20 -i S,1,0.50.
513 In order to create a custom SK1 genome to facilitate more accurate genotype-calling, SNP and indel
514 polymorphisms were detected using the GATK (GenomeAnalysisToolkit) function *HaplotypeCaller* (Van der
515 Auwera et al., 2013). An in-house script (*VariantCaller.pl*) subsequently parses the resulting VCF files from 72
516 spores to calculate: (i) the call frequency (% of spores any given allele is present within), (ii) the cumulative
517 allelic read depth (% of reads that contain a specific allele at a specific loci), and (iii) the cumulative total read
518 depth. To identify legitimate SNPs and indels, variants were filtered for a call-frequency between 44-55%, a
519 total read depth of >250 and an allelic read depth of 95%. Variants within repeat regions, long terminal repeats,
520 retrotransposons and telomeres were also discarded—yielding a final, robust list of 64,591 SNPs and 3972
521 indels amounting to ~0.57% divergence. A custom SK1 genome (SK1_Mod) was then generated by modifying
522 SacCer3 (v. R64-2-1) to include all filtered/called SNPs and indels.

523

524 **Genotype-Calling**

525 Spore data from individual samples was aligned to both the custom SK1_Mod genome and the SacCer3
526 reference (see below). Alignment produced a SAM file, which was converted into a sorted BAM file using the
527 Samtools function, *view* (Li et al., 2009), for downstream processing. The PySamStats (v. 1.0.1, Miles &
528 Mattioni) module, *variation*, was used to process the sorted BAM file for each sequenced spore, producing a
529 list of the number of reads containing A/C/T/G, insertion or deletion for each genomic position specified in the
530 S288c and SK1 references. Variant reads were isolated and genotyped using in-house, custom scripts as
531 follows. Genotypes were assigned according to the rules: (i) A minimum coverage-depth of 5; (ii) A SNP was
532 called as having the variant genotype if >=70% of the reads at that position match the called variant, or as
533 reference if =>90% of the reads match the reference; (iii) If the variant and reference reads were above 90%
534 of all reads and within 70% of each other, the position was called as heteroduplex; (iv) indels are called as
535 having the variant genotype if >=30% of the reads at that position matched the variant. Such a low threshold
536 was utilised because alignment of indel sequences is biased towards the reference, which means that they
537 are unlikely to be erroneously called as matching the variant genotype. For an indel to be called as the
538 reference genotype, >=95% of the reads must match the reference sequence and there must be fewer than
539 two reads matching the variant call. Any variants that fall below these thresholds were discarded. Genotype
540 calls were converted into a binary signal, either 1 for S288c or 0 for SK1.

541 **Event Calling**

542 Using the binarised input, chromosomes were split into segments with the same segregation pattern using
543 published scripts (Marsolier-Kergoat et al., 2018). Segment types (i.e. 1:7, 2:6, 2:6, 3:5, 4:4, 4:4*, 5:3, 6:2, 6:2*
544 or 7:1 as previously described (Martini et al., 2011; Marsolier-Kergoat et al., 2018) were also recorded.
545 Recombination events were subsequently called as being a set of segments located between two 4:4
546 segments longer than 1.5 kb (Marsolier-Kergoat et al., 2018). A 4:4 segment corresponds to a Mendelian
547 segregation profile, 5:3 and 3:5 segments to half-conversion tracts, and 6:2 and 2:6 segments to full conversion
548 tracts. Each recombination event can contain between 0–2 COs or NCOs. Events were additionally classified
549 by the number of chromatids involved (i.e. 1, 2, either sister or non-sister, 3, 4). To ensure compatibility with
550 our data-analysis pipeline, published binarised input data ("segFiles') from the S96 x YJM789 hybrid (Chen et
551 al., 2008; Mancera et al., 2008; Oke et al., 2014; Al-Sweel et al., 2017), were minimally processed to match
552 column naming, with spores from tetrads each duplicated to create a fake "octad". This conversion involved
553 no changes in data, only minimal reformatting. Recombination events were then called in the same way as for
554 SK1 x S288c octads generated for this study. Any small differences in CO and NCO counts and positions
555 between the resulting data and that published are likely, therefore, to be due to subtle differences in the event
556 calling criteria used (for example event merging thresholds).

557

558 **Event Position & Inter-Crossover Distances (ICDs)**

559 Crossover position, or "midpoint", is defined as the distance between the mid-points of the first and last
560 SNP/indel markers—an estimate of true event tract length. Inter-crossover distances (ICDs) were then
561 calculated as the distance (in bp) between successive CO midpoints.

562

563 **(γ)-Mixture Modelling**

564 Distributional analysis of CO distributions is complicated by the existence of non-interfering, Mus81-Mms4
565 class II COs—indistinguishable from interfering ZMM-dependent class I COs in our assay. In essence, meiotic
566 ICDs represent a heterogenous, mixed system (**Fig. 2b**) with unknown quantities of each subclass. Latent
567 variables (e.g. class II CO %) may, however, be inferred through probabilistic and statistical methods.
568 Expanding upon the use of the gamma (γ) distribution to model meiotic ICDs from this type of data (Chen et
569 al., 2008; Anderson et al., 2015), experimental data was deconvoluted by fitting two (γ) distributions—one for
570 each subclass of CO—via an expectation maximisation (EM) algorithm (MATLAB 2018a). EM is a commonly
571 applied method for iterative clustering and parameter estimation in mixed models (Do and Batzoglou, 2008).
572 Briefly, any given ICD was assigned a probability reflective of how likely it is to belong to one of the two sub-

distributions. Subsequently, sub-distributions were iteratively shifted, and data point identity was reassigned until a maximum likelihood (ML) solution was converged upon. One (γ) distribution is expected to yield a final (γ)(α) value of ~1.0 (class II, random), while the other is expected to produce a (γ)(α) value of >1.5 (class I, non-random), with their relative contributions to the overall mixture (i.e. the class I:class II ratio) is dependent upon genotype. To validate this approach, simulated ICD datasets of two component mixtures with known parameters, at variable sample sizes (S), were generated using *RecombineSim* and deconvoluted (**Supplementary Fig. 4b**; see below). As a measure of accuracy, the average % difference (N(%Δ)) between estimated and actual parameters was calculated. To calculate average percentage differences N(%Δ) generated by the simulation, each simulated mixture (at each sample size) was performed 100 times. Gamma-parameter estimates were obtained for each simulation. The parameters obtained each time were: γ(α)1, γ(β)1, γ(α)2, γ(β)2, and the proportional weight of the non-random gamma present in the mixture (W1). Estimated values of each parameter were then compared to the actual values used to generate the simulated mixture via the standard percentage difference formula: (|X1-X2| / [(X1+X2)/2])*100. This calculation was repeated for all five of the estimated parameters, with each averaged across the 100 repeats to obtain the final estimated percentage difference value for each parameter. Because final errors for each of the five parameters were found to be similar to one other within each trial, they were averaged to obtain a single N(%Δ) value (Supplementary Fig. S4b-c). Accuracy is dependent upon sample size (S) and to a lesser extent on the relative proportions of each subpopulation—and thus how likely a subpopulation is to be readily observed within the mixed population. For example, (γ) mixtures containing 10 or 25% class II COs exhibit average errors of 10.0% and 9.1% at (S) = 500 and 4.53% and 3.73% at (S) = 2000 respectively (**Supplementary Fig. 4c**). Experimental datasets range from (S) values of 354 to 3365, therefore reasonable error rates of ~<10% were expected.

A similar mixed-modelling approach (CODA) has been used to estimate relative proportions of mixed gamma populations for distributions of COs along multiple observations of a chromosome (Gauthier et al., 2011). Initial attempts to use this software failed presumably due to our low sample number. We circumvented this problem by concatenating the genome-wide set of inter-CO distances within a single meiosis to generate single pseudo (giant) chromosome encompassing, effectively, the entire yeast genome. Best-fit non-random gammas and proportions of the non-random (sprinkling) component were subsequently estimated as: Wild type (alpha = 3.4, proportion 0.28); *msh2*Δ (alpha = 3.9, proportion 0.11). Such estimates are similar to those obtained using our direct gamma mixture-modelling algorithm (e.g. **Fig. 2d**).

605 **Simulating patterns of class I and class II CO formation**

606 Randomised or mixed (class I + class II) ICD simulations were performed using a simulation platform
607 (*RecombineSim*) built in MATLAB 2018a. A typical simulation run is depicted in (**Supplementary Fig. 4a**). In
608 brief, virtual *S. cerevisiae* chromosomes are constructed as binned, numerical arrays at a 100 bp resolution
609 adjusted to reflect the limit of experimental detection governed by the leftmost and rightmost genetic markers
610 (SNPs/indels). Any given 100 bp bin possesses a numerical recombination potential (recom(P)), which governs
611 the ability of an interfering CO to successfully form at that site. Once formed within the simulation, class I COs
612 impose a zone of "interference", by altering recom(P) values in adjacent bins in a distance-dependent
613 manner—a similar principle to the beam-film model of CO interference (Zhang et al., 2014a). The exact shape
614 and width of interference imposed was determined by the best fit (γ) parameters (α, β) obtained from the MLE
615 mixture modelling (see above) for the genotype currently being simulated—and applied as a hazard function
616 (EQN 1.1):

617 $h(x) = \frac{PDF(x)}{1-CDF(x)}$ (1.1)

618 A hazard function describes the probability that, given a pre-existing CO at position x(0), another CO will form
619 at any given distance (x) away (Chen et al., 2008)—and thus is a natural representation of interference. A
620 fractional amount of class II COs that remain insensitive to recom(P) are introduced via the C_{PROB} parameter
621 where necessary as in gamma-sprinkling models (Copenhaver et al., 2002; Housworth and Stahl, 2003;
622 Housworth and Stahl, 2003; Falque et al., 2009). In order to closely match the in vivo datasets, simulated CO
623 events arising within 1.5 kb of one another were also merged, creating a single visible event at the midpoint.

624

625 To explore the impact that failed class I CO maturation may have on genome-wide patterns, simulations were
626 additionally performed in which, for a controlled (and variable) fraction of class I events, the class I event itself
627 was removed from the population of counted events only after implementation of interference around the site
628 of this precursor event. Such "failed-maturation" events are thus influenced by pre-existing patterns of
629 interference, and indeed influence the probability of flanking class I CO events that may arise later in the
630 simulation, but are not themselves counted, and thus do not contribute directly to the final pattern or frequency
631 of CO events reported.

632

633 In all cases, simulations (N = 10,000 cells) were iterated until the final frequency of visible COs (class I plus
634 class II) per simulated cell equaled the frequency observed for a given genotype. Thus, when events were

635 merged, and/or when events were removed (to simulate maturation failure), additional CO events were
636 simulated for those cells.
637
638 **ICD Transformation**
639 The formation of a variable number of events (N) within a finite space (*lim*) (i.e. a chromosome or genome
640 length) skews CDFs i.e. a higher CO frequency causes a downward shift in ICD size. An ICD distribution
641 produced under identical spatial rules but with a different event count would therefore generate significantly
642 different CDFs—failing or biasing statistical testing and undermining the ability to assess distributional
643 agreement. This skew can be readily observed using simulated data (**Supplementary Fig. 1a**). Notably, higher
644 values of (N) cause a leftward skew. The relationship between (N) and ICD size for a given *lim* is, however,
645 linear (Batten et al., 1993). Consequently, in order to isolate the distributional identity of any given sample (i.e.
646 isolate γ(α) from γ(β)), ICD data can be transformed by calculating the product of ICD size (ICD x event count).
647 Data transformation results in perfectly aligned CDFs despite varying (N), validating this approach
648 (**Supplementary Fig. 1b**).
649
650 **Statistical Analyses**
651 A *Kolmogorov-Smirnov* goodness-of-fit (GoF) test is a non-parametric test used to compare continuous
652 probability distributions in order to assess the null hypothesis that both samples derive from identical
653 populations, based on their maximal difference (D_{KS}) (Massey Jr, 1951; Miller, 1956). (P) values of the KS-test
654 effectively describe the probability that, if the null hypothesis is true, the observed CDFs would be as far apart
655 as observed. (P) values may therefore constitute an indirect measure of distributional agreement, as employed
656 throughout this paper. KS-tests were performed using the MATLAB 2018a packages: *kstest* and *kstest2*. A
657 two-sample T-test was utilised to determine whether a difference in mean value is significant or has arisen by
658 chance. Two-sample T-Tests were performed using the MATLAB 2018a package: *ttest2*.
659
660 **Microscopy and Cytological Analysis**
661 4.5 mL of meiotic culture was spun down on a bench centrifuge and resuspended to 500 µL with 1M pH 7.0
662 D-Sorbitol. 12 µL of 1.0 M DTT and 7 µL of 10 mg/mL Zymolyase in 10% glucose solution was added and cells
663 were spheroplasted by incubation at 37°C for 35–50 min with agitation. Spheroplasting success was
664 determined by taking 2–3 µL of the solution and adding an equivalent volume of 1.0% (w/v) Sodium N-
665 Lauroylsarcosine while under microscopic observation. Cells should immediately lyse as the exposed
666 membrane is disrupted by the detergent. 3.5 mL of Stop Solution (0.1M MES, 1 mM EDTA, 0.5 mM $MgCl_2$, 1M

667 D-Sorbitol, pH 6.4) was subsequently added and the cells were spun down to be resuspended in 100 µL
668 Spread Solution (0.1M MES, 1 mM EDTA, 0.5 mM $MgCl_2$, pH 6.4) and distributed between four slides, which
669 had been soaked in 70% ethanol overnight and wiped clean. To each slide, fixative (4.0% (w/v) formaldehyde,
670 3.8% (w/v) Sucrose, pH7.5) was added dropwise, followed by detergent (1% Lipsol, 0.1% Bibby Sterilin) to a
671 ratio of 1:3:6 (suspension : fixative : detergent) before lightly mixing and incubating for 1 min at room
672 temperature (RT). Further fixative was added dropwise to a final ratio of 1:9:6 and the mixture spread across
673 the slide. Each spread was subsequently incubated at RT for 30 min in damp conditions, then allowed to air
674 dry at RT overnight. Once dry, slides were sequentially washed in 0.2% (v/v) PhotoFlo Wetting Agent (Kodak)
675 and dH_2O, and stored at 4°C.
676
677 Slides were washed once in 0.025% Triton X-100 for 10 min at RT and twice in PBS for 5 min at room
678 temperature. Slides were blocked in 5% skimmed milk with PBS for 3 h at 37°C. Excess liquid was removed
679 and slides laid horizontally in damp conditions. 40 µL of primary antibody (anti-Zip3 (Shinohara et al., 2008)
680 from rat at 1:200 and/or anti-Red1 (Genecust, affinity purified, raised against aa(426-827)) from rabbit at 1:200)
681 in 1% skimmed milk with PBS was added under coverslips. Slides were incubated at 4°C overnight (15.5 h)
682 and washed three times in PBS for 5 min at RT. Excess liquid was then removed and slides were returned to
683 damp conditions. 40 µL of secondary antibody (anti-rat AlexaFluor555 at 1:200 and anti-rabbit AlexaFluor488
684 at 1:500) in 1% skimmed milk with PBS iwas added under coverslips. Slides were incubated at room
685 temperature for 2.5 h and then washed three times with PBS for 5 min at room temperature. Cover slips were
686 affixed using Vectashield mounting medium with DAPI, sealed with clear varnish and imaged on an Olympus
687 IX71 (z = 0.2 µM, Exposure times: TRITC-mCherry = 0.2 sec, eGFP = 1.0s, DAPI = 0.1s). Images were
688 randomised, deconvoluted via Huygens (software) and foci were automatically counted using an in-house
689 plugin for ImageJ (FindFoci) as previously described (Herbert et al., 2014), with an appropriate mask to discard
690 signals outside of nuclei. For Zip3 interfoci-distance scoring, pixels denoting the centre of each Zip3 focus, and
691 Zip1 ends, were manually selected along clearly separable bivalents as determined by Zip1-GFP signal (120-
692 156 bivalents per strain, error margin of approximately 1 pixel = 0.1 µm). These positions were selected using
693 the ImageJ segmented line tool and segment lengths were then calculated by macro, confirming agreement
694 with total length as measured by ImageJ standard tool.
695
696
697

698 ## Supplementary Discussion

699 **The *SK1-ML3* allele has a reduced capacity to generate CO interference**

700 As previously noted, wild type CO frequencies are higher within S96 x YJM789 than S288c x SK1 (91.4 vs
701 74.3 COs/meiosis) (**Fig. 1b; Supplementary Table 1**). Moreover, CO distributions deviate even further from
702 that expected for a random distribution in S96 x YJM789 ($p<0.01$; Two-sample KS test) (**Supplementary Fig.
703 2a**) consistent with the (γ)-mixture modelling results (**Fig. 2d**) suggesting that the class I CO fraction is greater
704 in S96 x YJM789 (75% vs. 67%). Molecular incompatibilities between certain alleles of the CO formation or
705 CO interference machinery may account for these cross-specific differences (Al-Sweel et al., 2017). To
706 investigate this hypothesis further, we analysed the frequency and distribution of COs within an *mlh3*Δ S288c
707 x YJM789 background containing ectopically expressed copies of the wild-type SK1 *MLH1* and *MLH3* alleles
708 (*SK1-MLH3*) (Al-Sweel et al., 2017). Remarkably, introduction of the SK1 alleles was sufficient to alter the
709 genome-wide pattern of COs, producing a relative distribution identical to that observed in the S288c x SK1
710 hybrid ($p = 0.91$; Two-sample KS Test) (**Supplementary Fig. 2b**). Surprisingly, despite this change in CO
711 distribution, introduction of the SK1 alleles did not significantly reduce CO frequency when compared to the
712 large pool of 51 wild-type S96 x YJM789 tetrads (90.9 COs vs 91.4 per meiosis) (**Supplementary Table 1**).
713 However, the observed frequency was significantly reduced relative to the subset (n=5) of S96 x YJM789
714 tetrads generated independently (100.4 vs. 90.9 COs per meiosis; $p < 0.01$; Two-sample T-test; (Chen et al.,
715 2008)). Collectively, these results suggest that, in some manner, the SK1 *MLH1* and/or *MLH3* alleles are
716 partially deficient in class I CO formation, and/or propagation and/or sensitivity to CO interference. However,
717 the much lower CO frequency observed within S288c x SK1 hybrids (74.3 COs per meiosis) cannot be fully
718 ascribed to the SK1 *MLH1* and/or *MLH3* alleles alone. In the context of this study, the relative inefficiency of
719 class I CO formation in the SK1 x S288c hybrid enhances the visibility of the *msh2*Δ-induced CO phenotype
720 relative to in the S96 x YJM789 hybrid (**Fig. 1c-d**).

721

722 **Zip3 foci located at the termini of Zip1-stained synapsed axes**

723 We noted that within our microscopic analysis of synapsed chromosomes a large proportion of Zip3 foci
724 appeared to occur at the terminal ends of Zip1 stretches (**Fig. 3c-d**). However, we suggest that this is less
725 likely to represent disproportionate Zip3 occupancy at chromosome ends than the presence of at least some
726 fraction of the chromosome length (i.e. telomere proximal) that is not visible in this assay—perhaps suggesting
727 that Zip1 loading and/or polymerisation beyond the most terminal Zip3 focus is inefficient and/or destabilised
728 during the spreading procedure. Indeed, in a similar analysis, Zhang *et al* (Zhang et al., 2014b) observed

729 telomeric LacO/LacI-GFP staining (on Chr. XV) beyond the end of the observable synaptonemal complex as
730 stained by Zip1. Such observations are also consistent with the observations that chromosome ends
731 disproportionately retain markers of incomplete synapsis and persistent DSB formation (Subramanian et al.,
732 2019), and have differential compaction that is Zip1-dependent (Schalbetter et al., 2019) at this *ndt80*Δ-induced
733 pachytene-arrest stage.
734

735 **Localised impact of polymorphism density upon CO formation**

736 S288c x SK1 variants have an average density of 1 per 175 bp and a median inter-variant distance of 81 bp
737 (93.12% of inter-variant distances are <500bp) and are therefore evenly spaced and present at high density
738 across each chromosome. Maps of polymorphism density are shown in (**Supplementary Fig. 7c-d**) for two
739 example chromosomes. In general, S288c x SK1 chromosomes are organised into local peaks and troughs of
740 variant density while maintaining overall uniformity. Therefore, it seems unlikely that inactivation of Msh2 would
741 result in a gross-redistribution of CO formation toward any particular region of the chromosome as it may do
742 within organisms with less uniform SNP/indel density, such as *A. thaliana* (Ziolkowski et al., 2015). To further
743 investigate the way in which polymorphisms sculpt the meiotic landscape, we repeated the analysis shown in
744 (**Fig. 4b-c**) using expanded ±1000 bp and ±2000 bp windows (**Supplementary Fig. 7a-b**). A Msh2-dependent
745 and statistically significant skew toward regions of lower sequence divergence ($p<0.01$; Two-sample KS test)
746 is retained at ±1000 bp but is significantly diminished at ±2000 bp ($p=0.51$; Two-sample KS test), suggesting
747 that mismatched sequences have the greatest impact when present within the recombination intermediate
748 structures.
749

750 ## Figure legends

751 **Fig. 1 | Inactivation of Msh2 increases CO frequency and the global strength of CO interference**

752 **a,** Genome-wide mapping of recombination. Meiosis is induced within hybrid S288c x SK1 *S. cerevisiae* diploid
753 cells and genomic material is prepped from individual, isolated spores for paired-end Illumina sequencing in
754 order to genotype SNP/indel patterns and therefore determine the parental origin of any given loci (**Methods**).
755 Only a single chromosome is shown for clarity. Inter-crossover distances (ICDs), a measure of the uniformity
756 of CO distribution, are calculated as the distance (in bp) between successive COs along a given chromosome.
757 **b,** Average number of COs per meioses for each genotype. The number of individual meioses sequenced per
758 genotype is indicated. Error bars: 95% confidence intervals (CI). P values: Two-sample T-test. **c-f,** Empirical
759 cumulative distribution functions (eCDFs) showing the fraction of ICDs at or below a given size. The total

number of experimental ICDs is indicated in brackets. ICDs are transformed (**Methods**) to correct for skews generated by differing CO frequencies. Untransformed ICD plots are available in (**Supplementary Fig. 1c-h**). Randomised datasets were generated via simulation to represent a state of no interference (Methods). Pairwise goodness-of-fit tests were performed between genotypes as indicated (triangular legend). P values: Two-sample KS-test.

Fig. 2 | Computational modelling predicts a Msh2-dependent shift in the class I:class II CO ratio

a, Ratio of experimentally observed ICD sizes (OBS) versus the theoretical expectation based on a single, best-fit gamma (γ)-distribution (EXP). Ratio values were calculated at 5 kb intervals. **b,** Example (γ) mixture model (α1.0|β1.0 + α3.0|β5.0). I = class I. II = class II. k datasets, owing to the existence of two CO subclasses, are a heterogenous population of three ICD types (as shown). **c,** As in **(a)** but based on a mixed (γ)-model (no. of distributions fitted = 2). **d,** Best-fit (γ) mixture modelling results. N = sample size (total number of ICDs). α_s = Single-fit γ(α) value. $P_{(s)}$ = Fit quality of a single (γ)-distribution (one-sample KS-test). αI, αII = Mixed model γ(α) values for each class. Class I, ClassII = estimated fraction of each CO subclass. Ratio = class I:class II. $P_{(M)}$ = Fit quality of a mixed (γ)-mode (Two-sample KS-test) **e-f,** Estimated class I and class II CO counts respectively. Estimates were obtained using the best-fit class I:class II ratios. Total CO frequencies are overlaid (grey bar). Error bars: 95% confidence intervals. The number of individual meioses sequenced per genotype is indicated.

Fig. 3 | Zip3 foci counts are neither elevated nor redistributed within Msh2-deficient cells

a, Box-and-whisker plot showing Zip3 foci counts obtained from chromosome spreads of S288c x SK1 *ndt80AR* cells prepared at 8 h following induction of meiosis (pachytene arrest). Midlines denote median values, box limits are first and third quartile, whiskers are highest/lowest values within 1.5-fold of interquartile range. P values: Two-sample T-test. **b,** Representative example for each genotype. Cells are fluorescently labelled for the meiosis-specific axis protein Zip1-GFP (green), the class I CO marker, Zip3 (red) and DNA (DAPI, blue). Only well-spread nuclei with clear Zip1 threads were analysed. Only Zip3 foci overlapping within the DAPI-stained area were counted. The total number of nuclei counted is indicated in brackets obtained from three independent experiments. **c-d,** Relative distribution of Zip3 foci along individual Zip1-GFP positive chromosome axes in *ndt80AR* and *msh2*Δ *ndt80AR* pachytene-arrested cells, ordered from bottom to top by increasing axis length (Green bar, measured Zip1 axis length; red dot Zip3 focus position). **e-f,** Inter-Zip3 foci distances (measured in microns) were aggregated, rank ordered, and expressed as a fraction of the total (i.e. an eCDF), equivalent to our presentation of inter-CO distances detected from octad sequencing data. In (**e**),

792 observed distributions are compared to simulations of the same number of randomly distributed foci over the
793 same total axial distance, using four increasingly stringent merging thresholds (0.05, 0.01, 0.15, and 0.2
794 microns; light grey to dark grey dashed lines) equivalent to approximate range of imaging resolution (1 pixel =
795 0.1 microns). Observed distributions were not statistically dissimilar in the presence and absence of Msh2, but
796 were significantly different from all simulated random distributions regardless of merging threshold. In (**f**), the
797 observed distributions are compared to a simulated gamma distribution, that whilst still statistically dissimilar,
798 shows a clear visual similarity. The residual deviation from an interfering gamma distribution may be caused
799 by inherent inaccuracies in microscopy resolution, or a real characteristic of Zip3 foci as measured along
800 spread chromosome axes.

801

802 **Fig. 4 | Suppression of class I COs occurs at regions of higher sequence divergence**

803 **a,** SNP/indel count is assayed using a ±500 bp window centred on CO or DSB hotspot midpoints. All contained
804 SNP/indels are tallied with equal weight. **b-c,** Empirical cumulative distribution functions (eCDFs) showing the
805 fraction of COs that reside within a region of a given SNP/indel count for S288c x SK1 (**b**) and S96 x YJM789
806 (**c**) for the indicated hybrid strains. Expected eCDF curve (grey) is calculated using DSB hotspot midpoints
807 (Pan et al 2011). Pairwise goodness-of-fit tests were performed between pooled *msh2*Δ and *MSH2* control
808 datasets as indicated (triangular legend). P values: Two-sample KS-test.

809

810 **Fig. 5 | Simulating impact of CO maturation failure on observed CO distributions.**

811 **a,** Extended *RecombineSim* platform as described in **Supplementary Fig. 4**, but with the introduction of
812 variable rates of stochastic class I CO maturation failure downstream of CO interference patterning in addition
813 to variable fractions of randomly distributed class II COs. In this simulation, class I COs that fail to mature are
814 still sensitive to, and still generate, localised regions of interference, but are removed from the final observed
815 pattern of visible events. In such instances, additional COs are simulated until the final observed simulated
816 frequency matches the frequency observed in experimental datasets. COs arising within 1.5 kb of one another
817 are merged into a single event, again matching the way experimental datasets are processed. **b-g,** Coloured
818 heat maps of P values (KS test) between observed and simulated CO distributions expressed as eCDF curves
819 for the indicated strains. P values >0.9 indicate good statistical fits. Each pixel represents a particular
820 combination of parameter values: maturation failure rate (Y axis) and class II CO % (X axis). See main text
821 and Methods for more details.

822

823

824 **Fig. 6 | Model summarising mismatch-directed suppression of class I COs**

825 **a-b,** Mismatches (jagged lines) may arise within recombination intermediates at various stages of the meiotic
826 recombination pathway due to differences in sequence between parental information A (blue) and B (red). **c,**
827 In the presence of a functional MMR pathway, regions of higher sequence divergence are proposed to give
828 rise to transient heteroduplexes that cause Msh2-dependent redirection of repair toward the NCO or inter-
829 sister outcomes. Formation of NCOs could arise via destabilisation of nascent strand-invasion intermediates,
830 dissolution of dHJs via Sgs1-Rmi1-Top3, or disruption of CO-biased dHJ resolution (see text for more details).
831 Concomitant repair of mismatches may additionally render some NCO events invisible, and thereby
832 indistinguishable from inter-sister events, due to restoration of parental markers. Inactivation of MMR alleviates
833 such repression arising within CO precursors, increasing the frequency of class I CO formation and thus the
834 spatial uniformity within relative CO positions. In the absence of pro-class I CO factors such as Zip3, Mlh1-3
835 and Msh4-5, class II COs can arise, but are less subject to Msh2-dependent destabilisation, perhaps due to
836 intrinsic differences in structure, lifespan, and/or extent of heteroduplex DNA. For example, extended branch
837 migration of Holliday junctions at class I precursors (Marsolier-Kergoat et al 2018) which may stabilise such
838 intermediates (Ahuja et al 2021) could increase the probability of hDNA arising within them, and thereby
839 increase Msh2-dependent redirection towards NCO outcomes.

840

841 **Supplementary Figure Legends**

842 **Supplementary Fig. 1 | CO interference is present to varying degrees within all mapped strains**

843 **a,** Empirical cumulative distribution function (eCDF) showing ICD data derived from interfering simulations
844 (γ(α) = 3.0) at varying CO per cell frequencies (N). **b,** As in **(a)** but ICDs are transformed (see **Methods**) to
845 correct for skews generated by differing CO frequencies. **c-h**, eCDFs showing the fraction of ICDs at or below
846 a given size. The total number of experimental ICDs is indicated in brackets. Randomised datasets were
847 generated via simulation to represent a state of no interference (**Methods**). Pairwise goodness-of-fit tests were
848 performed between genotypes as indicated (triangular legend). P values: Two-sample KS-test.

849

850 **Supplementary Fig. 2 | Cross-specific differences—the *SK1-MLH3* allele has reduced capacity to**
851 **mediate CO interference**

852 **a-b,** Empirical cumulative distribution functions (eCDFs) showing the fraction of ICDs at or below a given size.
853 The total number of experimental ICDs is indicated in brackets. ICDs are transformed (see **Methods**) to correct
854 for skews generated by differing CO frequencies. Randomised datasets were generated via simulation to
855 represent a state of no interference (**Methods**). Pairwise goodness-of-fit tests were performed between

genotypes as indicated (triangular legend). A schematic of the *SK1-MLH3* strain analysed is shown. P values: Two-sample KS-test. **c,** Average number of COs per meiosis for each genotype. P values: Two-sample T-test.

Supplementary Fig. 3 | Mechanistic details of MMR-dependent suppression of interfering COs

a, Empirical cumulative distribution function (eCDF) showing the fraction of ICDs at or below a given size. The total number of experimental ICDs is indicated in brackets. ICDs are transformed (see **Methods**) to correct for skews generated by differing CO frequencies. Randomised datasets were generated via simulation to represent a state of no interference (**Methods**). Pairwise goodness-of-fit tests were performed between genotypes as indicated (triangular legend). P values: Two-sample KS-test. **b,** Average number of COs per meiosis for each genotype. The number of individual meioses sequenced per genotype is indicated. Error bars: 95% confidence intervals (CI*). P values: Two-sample T-test.* **c-d,** As in **(a)** but for differing genotypes.

Supplementary Fig. 4 | Modelling CO distributions.

a, *RecombineSim* overview. Virtual chromosomes are constructed at a 100bp resolution as binned, numerical arrays upon which meiotic CO formation is simulated (**Methods**). Any given 100bp contains a value in the range of [0.0-1.0], designating its recombination potential (Rec(P)). Prior to CO formation, bins are initially populated with [1.0]—denoting an equal probability of class I CO formation in any given bin. During the formation of an interfering CO, *RecombineSim* imposes CO interference as a distance-dependent zone of repression by modifying Rec(P) values according to a hazard function derived from a manually specified $\gamma(\alpha_I)$ value, or a $\gamma(\alpha_I)$ value estimated from experimental data following gamma (γ) mixture modelling using maximum likelihood expectation (MLE; **Methods**). Such localised repression around each sequential event thus has the potential to influence the position of all subsequent interfering COs that are simulated. Non-interfering, class II COs are distributed randomly independently of Rec(P) and do not impose, nor are sensitive to, simulated CO interference. Successive events falling within a set threshold of one another (e.g. 1.5 kb) are merged into a single event residing at the midpoint position. These processes repeat until a pre-determined number of simulated ICDs are obtained. **b,** To estimate accuracy of the MLE mixture modelling algorithm, it was used to resolve and estimate individual components of simulated two component mixtures with known parameters (α, β), at known weights (W)—generated via *RecombineSim*. A set of representative examples are shown. Percentage differences between actual and estimated parameters are calculated and averaged to estimate error rate (N(%Δ)) and algorithm accuracy. S = number of ICDs. **c,** Error rate (N(%Δ)) values for three (γ) mixtures calculated at varying sample size (S).

Supplementary Fig. 5 | Specificity of anti-Zip3 antibody

a-b, Representative chromosome spreads of control (**a**) and *zip3*Δ (**b**) cells at the approximate pachytene stage of meiosis, indicated by Zip1-GFP thread-like signals in control cells, but more punctate Zip1-GFP patterns in *zip3*Δ cells (the most complete that they become). Occasional Zip1-GFP polycomplexes were also observed (arrowhead). In *zip3*Δ cells, anti-Zip3 staining detected only background random signals arising from random binding on the slides at locations that were not enriched in the areas of spread chromatin (blue DAPI-stained signals). Scale bar = µm

Supplementary Fig 6. Detected Zip3 foci counts are positively correlated with DAPI-delimited nuclear-spread area.

a, Scatter plot of Zip3 foci counts per cell against spread area delimited by the DAPI-positive signal for the indicated strains. R-squared correlation values are shown. **b,** Box-and-whisker plot showing Zip3 foci counts per square micron obtained from chromosome spreads of S288c x SK1 *ndt80*Δ cells prepared at 8 h following induction of meiosis (pachytene arrest). Midlines denote median values, box limits are first and third quartile, whiskers are highest/lowest values within 1.5-fold of interquartile range. P values: Two-sample T-test. The total number of nuclei counted is indicated in brackets.

Supplementary Fig. 7 | Localised impact of polymorphism density upon CO formation.

a-b, Empirical cumulative distribution functions (eCDFs) showing the fraction of COs that reside within a region (±1000bp and ±2000bp respectively) of a given SNP/indel count (S288c x SK1 only). Expected is calculated using DSB hotspot midpoints (Pan et al 2011). Pairwise goodness-of-fit tests were performed between pooled *msh2*Δ and *MSH2*$^{+}$ datasets as indicated (triangular legend). P values: Two-sample KS-test. **c-d,** Example smoothed SNP/INDEL density maps per 1 kb bin in the S288c x SK1 hybrid for ChrVI and ChrVII.

Supplementary Fig. 8 | Impact on simulated CO distributions of local deviations in density of heterozygosity, DSBs, and COs

a-b, Comparison of spatial distribution of population-average densities of heterozygosity, DSB formation (Pan et al. 2011), and CO formation in wild-type and *msh2*Δ cells for four representative chromosomes binned at 10 kb resolution. Although each chromosome has localised deviation from uniformity, each feature is spread relatively evenly across the length of each chromosome. **e-g,** To test the impact that localised deviations in heterozygosity (**e**), DSB formation (**f**), and observed CO density (**g**) might have on relative distributions of COs, simulations of example random (RND; alpha=1) and interfering (INT; alpha=3) gamma distributions were

performed as in **Supplementary Fig. 4**, but additionally weighting CO site selection by the relative amplitude of each parameter at varying levels of smoothing (0.1–25 kb). No change in distributions were observed indicating that the nonuniform distribution of these features is unable to significantly bias relative patterns of CO formation. P values reported are the minimum observed out of the five smoothing values tested for each parameter.

References

Agarwal, S., and Roeder, G. S. (2000). Zip3 provides a link between recombination enzymes and synaptonemal complex proteins. Cell *102*, 245-255.

Ahuja, J. S., Harvey, C. S., Wheeler, D. L., and Lichten, M. (2021). Repeated strand invasion and extensive branch migration are hallmarks of meiotic recombination. Mol Cell *81*, 4258-4270.e4.

Al-Sweel, N., Raghavan, V., Dutta, A., Ajith, V. P., Di Vietro, L., Khondakar, N., Manhart, C. M., Surtees, J. A., Nishant, K. T., and Alani, E. (2017). mlh3 mutations in baker's yeast alter meiotic recombination outcomes by increasing noncrossover events genome-wide. PLoS Genet *13*, e1006974.

Alani, E., Lee, S., Kane, M. F., Griffith, J., and Kolodner, R. D. (1997). Saccharomyces cerevisiae MSH2, a mispaired base recognition protein, also recognizes Holliday junctions in DNA. J Mol Biol *265*, 289-301.

Allers, T., and Lichten, M. (2001). Differential timing and control of noncrossover and crossover recombination during meiosis. Cell *106*, 47-57.

Anderson, C. M., Oke, A., Yam, P., Zhuge, T., and Fung, J. C. (2015). Reduced Crossover Interference and Increased ZMM-Independent Recombination in the Absence of Tel1/ATM. PLoS Genet *11*, e1005478.

Batten, L. M., Batten, L. M., and Beutelspacher, A. (1993). The Theory of Finite Linear Spaces Cambridge University Press).

Baudat, F., and de Massy, B. (2007a). Regulating double-stranded DNA break repair towards crossover or non-crossover during mammalian meiosis. Chromosome Res *15*, 565-577.

Baudat, F., and de Massy, B. (2007b). Cis- and trans-acting elements regulate the mouse Psmb9 meiotic recombination hotspot. PLoS Genet *3*, e100.

Benjamin, K. R., Zhang, C., Shokat, K. M., and Herskowitz, I. (2003). Control of landmark events in meiosis by the CDK Cdc28 and the meiosis-specific kinase Ime2. Genes Dev *17*, 1524-1539.

Berchowitz, L. E., and Copenhaver, G. P. (2010). Genetic interference: don't stand so close to me. Curr Genomics *11*, 91-102.

Bishop, D. K., and Zickler, D. (2004). Early decision; meiotic crossover interference prior to stable strand exchange and synapsis. Cell *117*, 9-15.

Blackwell, A. R., Dluzewska, J., Szymanska-Lejman, M., Desjardins, S., Tock, A. J., Kbiri, N., Lambing, C., Lawrence, E. J., Bieluszewski, T., Rowan, B., Higgins, J. D., Ziolkowski, P. A., and Henderson, I. R. (2020). MSH2 shapes the meiotic crossover landscape in relation to interhomolog polymorphism in Arabidopsis. EMBO J *39*, e104858.

Bozdag, G. O., Ono, J., Denton, J. A., Karakoc, E., Hunter, N., Leu, J. Y., and Greig, D. (2021). Breaking a species barrier by enabling hybrid recombination. Curr Biol *31*, R180-R181.

Cannavo, E., Sanchez, A., Anand, R., Ranjha, L., Hugener, J., Adam, C., Acharya, A., Weyland, N., Aran-Guiu, X., Charbonnier, J. B., Hoffmann, E. R., Borde, V., Matos, J., and Cejka, P. (2020). Regulation of the MLH1-MLH3 endonuclease in meiosis. Nature *586*, 618-622.

Chambers, S. R., Hunter, N., Louis, E. J., and Borts, R. H. (1996). The mismatch repair system reduces meiotic homeologous recombination and stimulates recombination-dependent chromosome loss. Molecular and cellular biology *16*, 6110-6120.

Chen, S. Y., Tsubouchi, T., Rockmill, B., Sandler, J. S., Richards, D. R., Vader, G., Hochwagen, A., Roeder, G. S., and Fung, J. C. (2008). Global analysis of the meiotic crossover landscape. Dev Cell *15*, 401-415.

Cole, F., Keeney, S., and Jasin, M. (2010). Comprehensive, fine-scale dissection of homologous recombination outcomes at a hot spot in mouse meiosis. Mol Cell *39*, 700-710.

Copenhaver, G. P., Housworth, E. A., and Stahl, F. W. (2002). Crossover interference in Arabidopsis. Genetics *160*, 1631-1639.

969 Crawford, M., Cooper, T. J., Marsolier-Kergoat, M.-C., Llorente, B., and Neale, M. J. (2018). Separable roles of the DNA
970 damage response kinase Mec1(ATR) and its activator Rad24(RAD17) within the regulation of meiotic recombination.
971 bioRxiv

972 de los Santos, T., Hunter, N., Lee, C., Larkin, B., Loidl, J., and Hollingsworth, N. M. (2003). The Mus81/Mms4
973 endonuclease acts independently of double-Holliday junction resolution to promote a distinct subset of crossovers during
974 meiosis in budding yeast. Genetics *164*, 81-94.

975 Do, C. B., and Batzoglou, S. (2008). What is the expectation maximization algorithm. Nat Biotechnol *26*, 897-899.

976 Engel, S. R., and Cherry, J. M. (2013). The new modern era of yeast genomics: community sequencing and the resulting
977 annotation of multiple Saccharomyces cerevisiae strains at the Saccharomyces Genome Database. Database (Oxford)
978 *2013*, bat012.

979 Falque, M., Anderson, L. K., Stack, S. M., Gauthier, F., and Martin, O. C. (2009). Two types of meiotic crossovers coexist
980 in maize. Plant Cell *21*, 3915-3925.

981 Gauthier, F., Martin, O. C., and Falque, M. (2011). CODA (crossover distribution analyzer): quantitative characterization
982 of crossover position patterns along chromosomes. BMC Bioinformatics *12*, 27.

983 Getz, T. J., Banse, S. A., Young, L. S., Banse, A. V., Swanson, J., Wang, G. M., Browne, B. L., Foss, H. M., and Stahl, F.
984 W. (2008). Reduced mismatch repair of heteroduplexes reveals “non”-interfering crossing over in wild-type
985 Saccharomyces cerevisiae. Genetics *178*, 1251-1269.

986 Goldfarb, T., and Alani, E. (2005). Distinct roles for the Saccharomyces cerevisiae mismatch repair proteins in
987 heteroduplex rejection, mismatch repair and nonhomologous tail removal. Genetics *169*, 563-574.

988 Goldstein, A. L., and McCusker, J. H. (1999). Three new dominant drug resistance cassettes for gene disruption in
989 Saccharomyces cerevisiae. Yeast *15*, 1541-1553.

990 Gray, S., and Cohen, P. E. (2016). Control of Meiotic Crossovers: From Double-Strand Break Formation to Designation.
991 Annu Rev Genet

992 Greig, D., Travisano, M., Louis, E. J., and Borts, R. H. (2003). A role for the mismatch repair system during incipient
993 speciation in Saccharomyces. J Evol Biol *16*, 429-437.

994 Harfe, B. D., and Jinks-Robertson, S. (2000). DNA mismatch repair and genetic instability. Annu Rev Genet *34*, 359-399.

995 Henderson, K. A., and Keeney, S. (2004). Tying synaptonemal complex initiation to the formation and programmed
996 repair of DNA double-strand breaks. Proc Natl Acad Sci U S A *101*, 4519-4524.

997 Herbert, A. D., Carr, A. M., and Hoffmann, E. (2014). FindFoci: a focus detection algorithm with automated parameter
998 training that closely matches human assignments, reduces human inconsistencies and increases speed of analysis.
999 PLoS One *9*, e114749.

1000 Holloway, J. K., Booth, J., Edelmann, W., McGowan, C. H., and Cohen, P. E. (2008). MUS81 generates a subset of
1001 MLH1-MLH3-independent crossovers in mammalian meiosis. PLoS Genet *4*, e1000186.

1002 Housworth, E. A., and Stahl, F. W. (2003). Crossover interference in humans. Am J Hum Genet *73*, 188-197.

1003 Hunter, N., Chambers, S. R., Louis, E. J., and Borts, R. H. (1996). The mismatch repair system contributes to meiotic
1004 sterility in an interspecific yeast hybrid. The EMBO journal *15*, 1726-1733.

1005 Jeffreys, A. J., and Neumann, R. (2005). Factors influencing recombination frequency and distribution in a human meiotic
1006 crossover hotspot. Hum Mol Genet *14*, 2277-2287.

1007 Kane, S. M., and Roth, R. (1974). Carbohydrate metabolism during ascospore development in yeast. J Bacteriol *118*, 8-
1008 14.

1009 Kaur, H., De Muyt, A., and Lichten, M. (2015). Top3-Rmi1 DNA Single-Strand Decatenase Is Integral to the Formation
1010 and Resolution of Meiotic Recombination Intermediates. Molecular Cell *57*, 583-594.

1011 Kolodner, R. D., and Marsischky, G. T. (1999). Eukaryotic DNA mismatch repair. Curr Opin Genet Dev *9*, 89-96.

1012 Kulkarni, D. S., Owens, S. N., Honda, M., Ito, M., Yang, Y., Corrigan, M. W., Chen, L., Quan, A. L., and Hunter, N.
1013 (2020). PCNA activates the MutLγ endonuclease to promote meiotic crossing over. Nature *586*, 623-627.

1014 Lam, I., and Keeney, S. (2015). Mechanism and regulation of meiotic recombination initiation. Cold Spring Harb Perspect
1015 Biol *7*, a016634.

1016 Langmead, B., and Salzberg, S. L. (2012). Fast gapped-read alignment with Bowtie 2. Nat Methods *9*, 357-359.

1017 Li, G. M. (2008). Mechanisms and functions of DNA mismatch repair. Cell Res *18*, 85-98.

1018 Li, H., Handsaker, B., Wysoker, A., Fennell, T., Ruan, J., Homer, N., Marth, G., Abecasis, G., Durbin, R., and 1000, G. P.
1019 D. P. S. (2009). The Sequence Alignment/Map format and SAMtools. Bioinformatics *25*, 2078-2079.

1020 Li, R., Bitoun, E., Altemose, N., Davies, R. W., Davies, B., and Myers, S. R. (2019). A high-resolution map of non-
1021 crossover events reveals impacts of genetic diversity on mammalian meiotic recombination. Nat Commun *10*, 3900.

Longtine, M. S., McKenzie, A., Demarini, D. J., Shah, N. G., Wach, A., Brachat, A., Philippsen, P., and Pringle, J. R. (1998). Additional modules for versatile and economical PCR-based gene deletion and modification in Saccharomyces cerevisiae. Yeast *14*, 953-961.

Lynn, A., Soucek, R., and Borner, G. V. (2007). ZMM proteins during meiosis: crossover artists at work. Chromosome Res *15*, 591-605.

Mancera, E., Bourgon, R., Brozzi, A., Huber, W., and Steinmetz, L. M. (2008). High-resolution mapping of meiotic crossovers and non-crossovers in yeast. Nature *454*, 479-485.

Mancera, E., Bourgon, R., Huber, W., and Steinmetz, L. M. (2011). Genome-wide survey of post-meiotic segregation during yeast recombination. Genome Biol *12*, R36.

Marsolier-Kergoat, M. C., Khan, M. M., Schott, J., Zhu, X., and Llorente, B. (2018). Mechanistic View and Genetic Control of DNA Recombination during Meiosis. Mol Cell *70*, 9-20.e6.

Martini, E., Diaz, R. L., Hunter, N., and Keeney, S. (2006). Crossover homeostasis in yeast meiosis. Cell *126*, 285-295.

Martini, E., Borde, V., Legendre, M., Audic, S., Regnault, B., Soubigou, G., Dujon, B., and Llorente, B. (2011). Genome-wide analysis of heteroduplex DNA in mismatch repair-deficient yeast cells reveals novel properties of meiotic recombination pathways. PLoS Genet *7*, e1002305.

Massey Jr, F. J. (1951). The Kolmogorov-Smirnov test for goodness of fit. Journal of the American statistical Association *46*, 68-78.

Matos, J., Blanco, M. G., Maslen, S., Skehel, J. M., and West, S. C. (2011). Regulatory control of the resolution of DNA recombination intermediates during meiosis and mitosis. Cell *147*, 158-172.

McPeek, M. S., and Speed, T. P. (1995). Modeling interference in genetic recombination. Genetics *139*, 1031-1044.

Miller, L. H. (1956). Table of percentage points of Kolmogorov statistics. Journal of the American Statistical Association *51*, 111-121.

Mortimer, R. K., and Johnston, J. R. (1986). Genealogy of principal strains of the yeast genetic stock center. Genetics *113*, 35-43.

Mu, X., Murakami, H., Mohibullah, N., and Keeney, S. (2020). Chromosome-autonomous feedback down-regulates meiotic DNA break competence upon synaptonemal complex formation. Genes Dev *34*, 1605-1618.

Oh, S. D., Lao, J. P., Hwang, P. Y., Taylor, A. F., Smith, G. R., and Hunter, N. (2007). BLM ortholog, Sgs1, prevents aberrant crossing-over by suppressing formation of multichromatid joint molecules. Cell *130*, 259-272.

Oke, A., Anderson, C. M., Yam, P., and Fung, J. C. (2014). Controlling meiotic recombinational repair - specifying the roles of ZMMs, Sgs1 and Mus81/Mms4 in crossover formation. PLoS Genet *10*, e1004690.

Pan, J., Sasaki, M., Kniewel, R., Murakami, H., Blitzblau, H. G., Tischfield, S. E., Zhu, X., Neale, M. J., Jasin, M., Socci, N. D., Hochwagen, A., and Keeney, S. (2011). A Hierarchical Combination of Factors Shapes the Genome-wide Topography of Yeast Meiotic Recombination Initiation. Cell *144*, 719-731.

Pannafino, G., and Alani, E. (2021). Coordinated and Independent Roles for MLH Subunits in DNA Repair. Cells *10*,

Peterson, S. E., Keeney, S., and Jasin, M. (2020). Mechanistic Insight into Crossing over during Mouse Meiosis. Mol Cell *78*, 1252-1263.e3.

Prolla, T. A., Pang, Q., Alani, E., Kolodner, R. D., and Liskay, R. M. (1994). MLH1, PMS1, and MSH2 interactions during the initiation of DNA mismatch repair in yeast. Science *265*, 1091-1093.

Reenan, R. A., and Kolodner, R. D. (1992). Isolation and characterization of two Saccharomyces cerevisiae genes encoding homologs of the bacterial HexA and MutS mismatch repair proteins. Genetics *132*, 963-973.

Rogacheva, M. V., Manhart, C. M., Chen, C., Guarne, A., Surtees, J., and Alani, E. (2014). Mlh1-Mlh3, A Meiotic Crossover and DNA Mismatch Repair Factor, is a Msh2-Msh3-Stimulated Endonuclease. J Biol Chem

Sarbajna, S., Davies, D., and West, S. C. (2014). Roles of SLX1-SLX4, MUS81-EME1, and GEN1 in avoiding genome instability and mitotic catastrophe. Genes Dev *28*, 1124-1136.

Schalbetter, S. A., Fudenberg, G., Baxter, J., Pollard, K. S., and Neale, M. J. (2019). Principles of meiotic chromosome assembly revealed in S. cerevisiae. Nat Commun *10*, 4795.

Shinohara, M., Oh, S. D., Hunter, N., and Shinohara, A. (2008). Crossover assurance and crossover interference are distinctly regulated by the ZMM proteins during yeast meiosis. Nat Genet *40*, 299-309.

Spies, M., and Fishel, R. (2015). Mismatch repair during homologous and homeologous recombination. Cold Spring Harb Perspect Biol *7*, a022657.

Srivatsan, A., Bowen, N., and Kolodner, R. D. (2014). Mispair-specific recruitment of the Mlh1-Pms1 complex identifies repair substrates of the Saccharomyces cerevisiae Msh2-Msh3 complex. J Biol Chem *289*, 9352-9364.

Storlazzi, A., Xu, L., Cao, L., and Kleckner, N. (1995). Crossover and noncrossover recombination during meiosis: timing and pathway relationships. Proc Natl Acad Sci U S A *92*, 8512-8516.

Subramanian, V. V., Zhu, X., Markowitz, T. E., Vale-Silva, L. A., San-Segundo, P. A., Hollingsworth, N. M., Keeney, S., and Hochwagen, A. (2019). Persistent DNA-break potential near telomeres increases initiation of meiotic recombination on short chromosomes. Nat Commun *10*, 970.

Sugawara, N., Goldfarb, T., Studamire, B., Alani, E., and Haber, J. E. (2004). Heteroduplex rejection during single-strand annealing requires Sgs1 helicase and mismatch repair proteins Msh2 and Msh6 but not Pms1. Proc Natl Acad Sci U S A *101*, 9315-9320.

Tang, S., Wu, M., Zhang, R., and Hunter, N. (2015). Pervasive and Essential Roles of the Top3-Rmi1 Decatenase Orchestrate Recombination and Facilitate Chromosome Segregation in Meiosis. Molecular Cell *57*, 607-621.

Thacker, D., Mohibullah, N., Zhu, X., and Keeney, S. (2014). Homologue engagement controls meiotic DNA break number and distribution. Nature *510*, 241-246.

Van der Auwera, G. A., Carneiro, M. O., Hartl, C., Poplin, R., Del Angel, G., Levy-Moonshine, A., Jordan, T., Shakir, K., Roazen, D., Thibault, J., Banks, E., Garimella, K. V., Altshuler, D., Gabriel, S., and DePristo, M. A. (2013). From FastQ data to high confidence variant calls: the Genome Analysis Toolkit best practices pipeline. Curr Protoc Bioinformatics *43*, 11.10.1-33.

Wang, S., Hassold, T., Hunt, P., White, M. A., Zickler, D., Kleckner, N., and Zhang, L. (2017). Inefficient Crossover Maturation Underlies Elevated Aneuploidy in Human Female Meiosis. Cell *168*, 977-989.e17.

White, E. J., Cowan, C., Cande, W. Z., and Kaback, D. B. (2004). In vivo analysis of synaptonemal complex formation during yeast meiosis. Genetics *167*, 51-63.

Xu, L., Ajimura, M., Padmore, R., Klein, C., and Kleckner, N. (1995). NDT80, a meiosis-specific gene required for exit from pachytene in Saccharomyces cerevisiae. Mol Cell Biol *15*, 6572-6581.

Zakharyevich, K., Tang, S., Ma, Y., and Hunter, N. (2012). Delineation of joint molecule resolution pathways in meiosis identifies a crossover-specific resolvase. Cell *149*, 334-347.

Zhai, J., and Hingorani, M. M. (2010). Saccharomyces cerevisiae Msh2-Msh6 DNA binding kinetics reveal a mechanism of targeting sites for DNA mismatch repair. Proc Natl Acad Sci U S A *107*, 680-685.

Zhang, L., Liang, Z., Hutchinson, J., and Kleckner, N. (2014a). Crossover patterning by the beam-film model: analysis and implications. PLoS Genet *10*, e1004042.

Zhang, L., Wang, S., Yin, S., Hong, S., Kim, K. P., and Kleckner, N. (2014b). Topoisomerase II mediates meiotic crossover interference. Nature *511*, 551-556.

Ziolkowski, P. A., Berchowitz, L. E., Lambing, C., Yelina, N. E., Zhao, X., Kelly, K. A., Choi, K., Ziolkowska, L., June, V., Sanchez-Moran, E., Franklin, C., Copenhaver, G. P., and Henderson, I. R. (2015). Juxtaposition of heterozygous and homozygous regions causes reciprocal crossover remodelling via interference during Arabidopsis meiosis. Elife *4*,

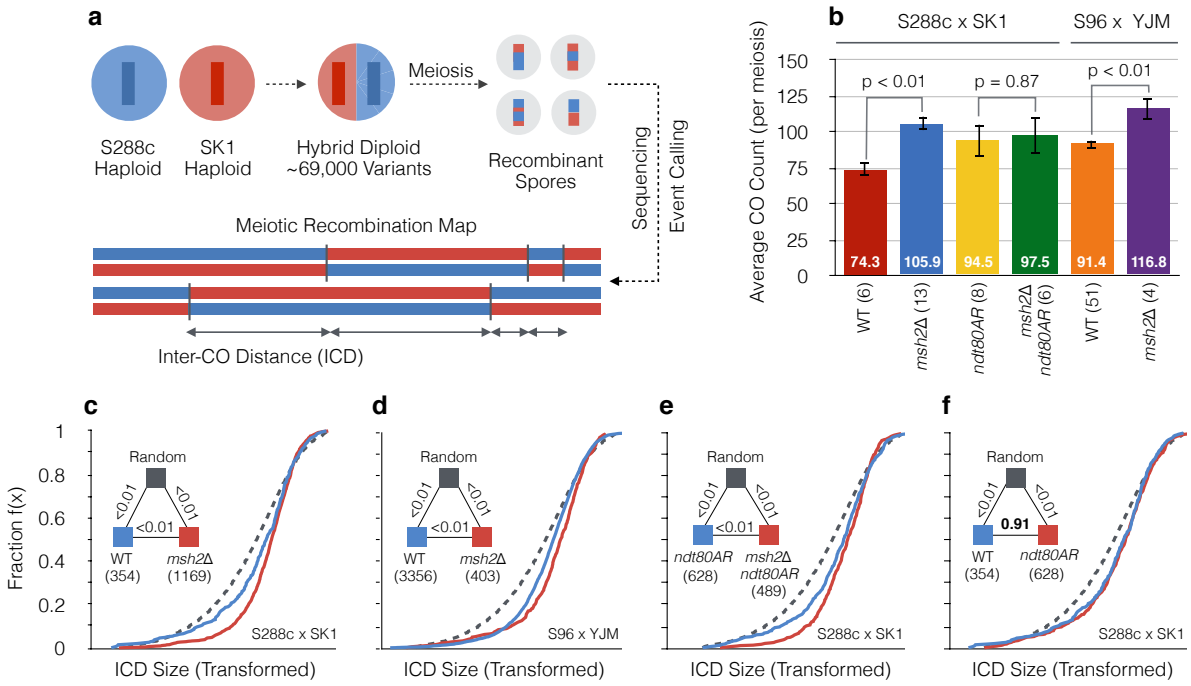

Fig. 1 | Inactivation of Msh2 increases CO frequency and the global strength of CO interference

a, Genome-wide mapping of recombination. Meiosis is induced within hybrid S288c x SK1 *S. cerevisiae* diploid cells and genomic material is prepped from individual, isolated spores for paired-end Illumina sequencing in order to genotype SNP/indel patterns and therefore determine the parental origin of any given loci (**Methods**). Only a single chromosome is shown for clarity. Inter-crossover distances (ICDs), a measure of the uniformity of CO distribution, are calculated as the distance (in bp) between successive COs along a given chromosome. **b,** Average number of COs per meioses for each genotype. The number of individual meioses sequenced per genotype is indicated. Error bars: 95% confidence intervals (CI). P values: Two-sample T-test. **c-f,** Empirical cumulative distribution functions (eCDFs) showing the fraction of ICDs at or below a given size. The total number of experimental ICDs is indicated in brackets. ICDs are transformed (**Methods**) to correct for skews generated by differing CO frequencies. Untransformed ICD plots are available in (**Supplementary Fig. 1c-h**). Randomised datasets were generated via simulation to represent a state of no interference (Methods). Pairwise goodness-of-fit tests were performed between genotypes as indicated (triangular legend). P values: Two-sample KS-test.

FIGURE 1

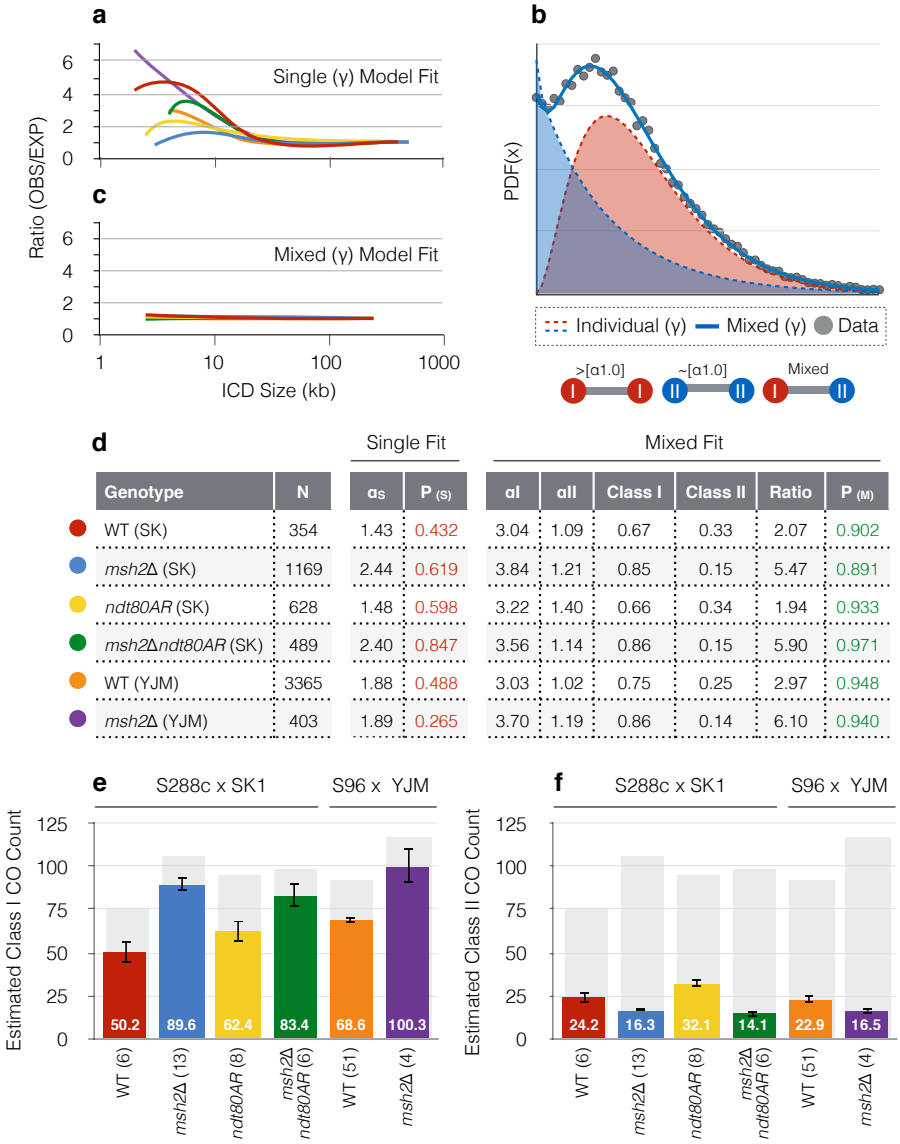

Genotype	N	α_S	$P_{(S)}$	αI	αII	Class I	Class II	Ratio	$P_{(M)}$
WT (SK)	354	1.43	0.432	3.04	1.09	0.67	0.33	2.07	0.902
*msh2*Δ (SK)	1169	2.44	0.619	3.84	1.21	0.85	0.15	5.47	0.891
ndt80AR (SK)	628	1.48	0.598	3.22	1.40	0.66	0.34	1.94	0.933
*msh2*Δ*ndt80AR* (SK)	489	2.40	0.847	3.56	1.14	0.86	0.15	5.90	0.971
WT (YJM)	3365	1.88	0.488	3.03	1.02	0.75	0.25	2.97	0.948
*msh2*Δ (YJM)	403	1.89	0.265	3.70	1.19	0.86	0.14	6.10	0.940

Fig. 2 | Computational modelling predicts a Msh2-dependent shift in the class I:class II CO ratio

a, Ratio of experimentally observed ICD sizes (OBS) versus the theoretical expectation based on a single, best-fit gamma (γ)-distribution (EXP). Ratio values were calculated at 5 kb intervals. **b,** Example (γ) mixture model (α1.0|β1.0 + α3.0|β5.0). I = class I. II = class II. k datasets, owing to the existence of two CO subclasses, are a heterogenous population of three ICD types (as shown). **c,** As in **(a)** but based on a mixed (γ)-model (no. of distributions fitted = 2). **d,** Best-fit (γ) mixture modelling results. N = sample size (total number of ICDs). α_s = Single-fit γ(α) value. $P_{(s)}$ = Fit quality of a single (γ)-distribution (one-sample KS-test). αI, αII = Mixed model γ(α) values for each class. Class I, ClassII = estimated fraction of each CO subclass. Ratio = class I:class II. $P_{(M)}$ = Fit quality of a mixed (γ)-mode (Two-sample KS-test) **e-f,** Estimated class I and class II CO counts respectively. Estimates were obtained using the best-fit class I:class II ratios. Total CO frequencies are overlaid (grey bar). Error bars: 95% confidence intervals. The number of individual meioses sequenced per genotype is indicated.

FIGURE 2

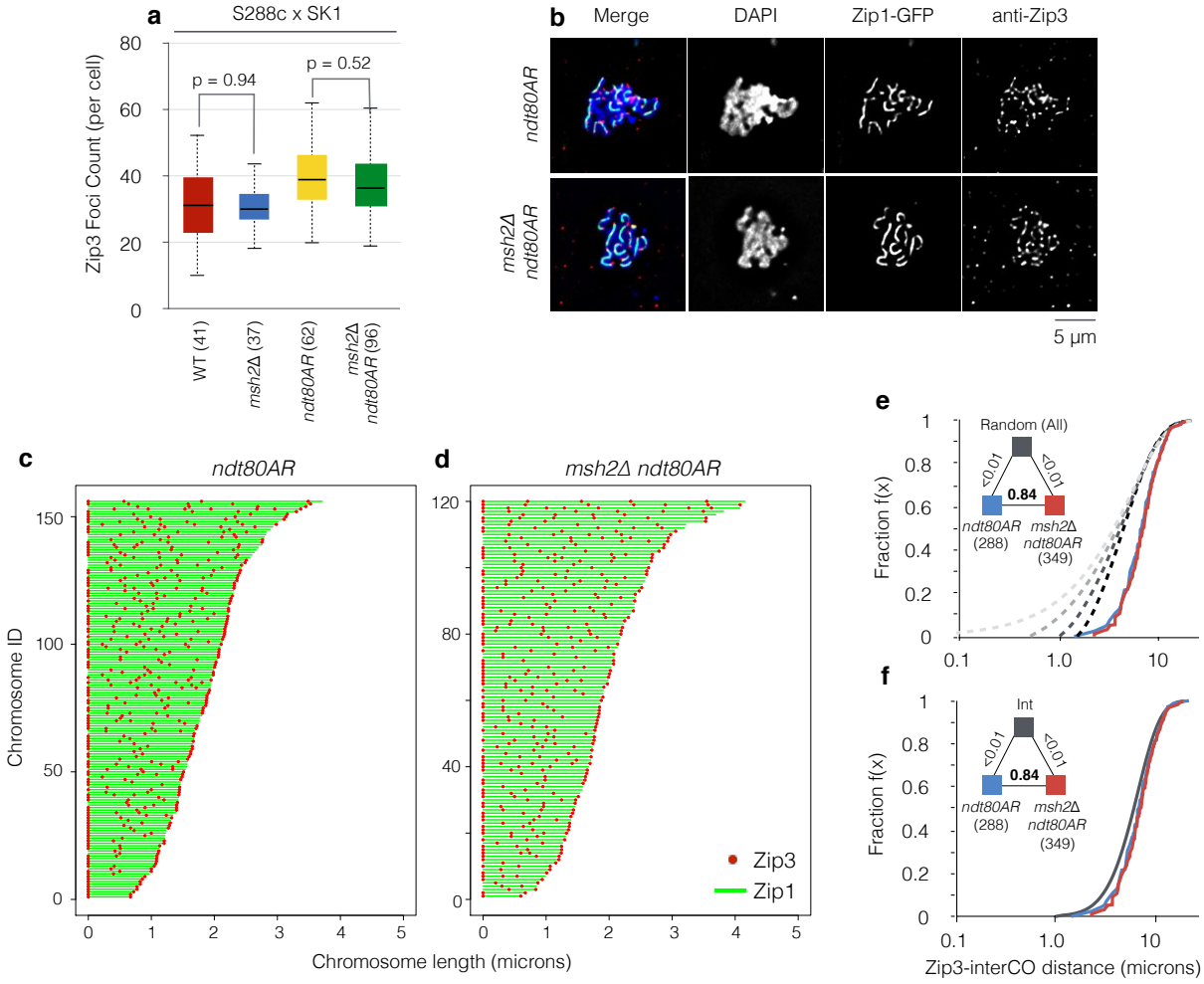

Fig. 3 | Zip3 foci counts are neither elevated nor redistributed within Msh2-deficient cells

a, Box-and-whisker plot showing Zip3 foci counts obtained from chromosome spreads of S288c x SK1 *ndt80AR* cells prepared at 8 h following induction of meiosis (pachytene arrest). Midlines denote median values, box limits are first and third quartile, whiskers are highest/lowest values within 1.5-fold of interquartile range. P values: Two-sample T-test. **b,** Representative example for each genotype. Cells are fluorescently labelled for the meiosis-specific axis protein Zip1-GFP (green), the class I CO marker, Zip3 (red) and DNA (DAPI, blue). Only well-spread nuclei with clear Zip1 threads were analysed. Only Zip3 foci overlapping within the DAPI-stained area were counted. The total number of nuclei counted is indicated in brackets obtained from three independent experiments. **c-d,** Relative distribution of Zip3 foci along individual Zip1-GFP positive chromosome axes in *ndt80AR* and *msh2Δ ndt80AR* pachytene-arrested cells, ordered from bottom to top by increasing axis length (Green bar, measured Zip1 axis length; red dot Zip3 focus position). **e-f,** Inter-Zip3 foci distances (measured in microns) were aggregated, rank ordered, and expressed as a fraction of the total (i.e. an eCDF), equivalent to our presentation of inter-CO distances detected from octad sequencing data. In (**e**), observed distributions are compared to simulations of the same number of randomly distributed foci over the same total axial distance, using four increasingly stringent merging thresholds (0.05, 0.01, 0.15, and 0.2 microns; light grey to dark grey dashed lines) equivalent to approximate range of imaging resolution (1 pixel = 0.1 microns). Observed distributions were not statistically dissimilar in the presence and absence of Msh2, but were significantly different from all simulated random distributions regardless of merging threshold. In (**f**), the observed distributions are compared to a simulated gamma distribution, that whilst still statistically dissimilar, shows a clear visual similarity. The residual deviation from an interfering gamma distribution may be caused by inherent inaccuracies in microscopy resolution, or a real characteristic of Zip3 foci as measured along spread chromosome axes.

FIGURE 3

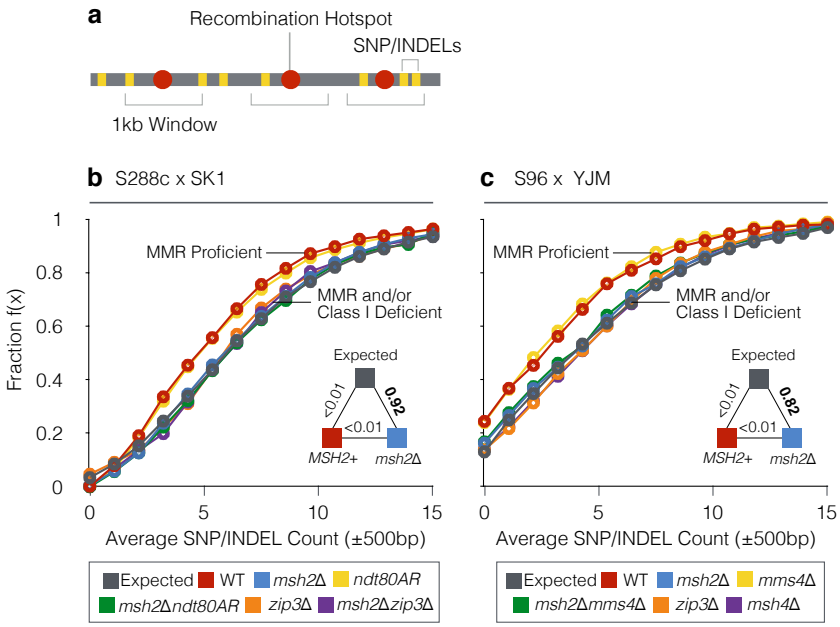

Fig. 4 | Suppression of class I COs occurs at regions of higher sequence divergence

a, SNP/indel count is assayed using a ±500 bp window centred on CO or DSB hotspot midpoints. All contained SNP/indels are tallied with equal weight. **b-c,** Empirical cumulative distribution functions (eCDFs) showing the fraction of COs that reside within a region of a given SNP/indel count for S288c x SK1 (**b**) and S96 x YJM789 (**c**) for the indicated hybrid strains. Expected eCDF curve (grey) is calculated using DSB hotspot midpoints (Pan et al 2011). Pairwise goodness-of-fit tests were performed between pooled *msh2*Δ and *MSH2* control datasets as indicated (triangular legend). P values: Two-sample KS-test.

FIGURE 4

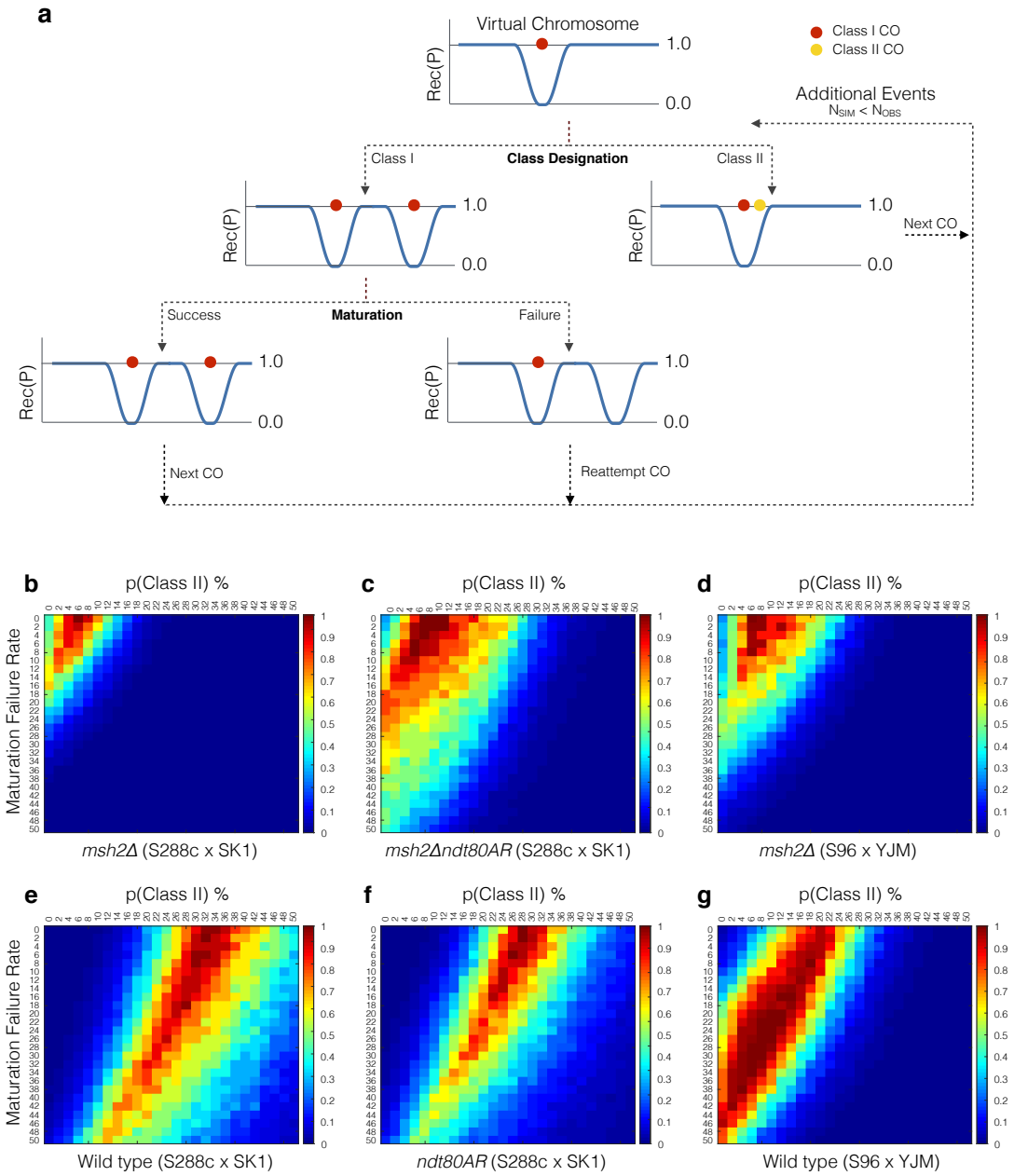

Fig. 5 | Simulating impact of CO maturation failure on observed CO distributions.

a, Extended *RecombineSim* platform as described in Supplementary Fig. 4, but with the introduction of variable rates of stochastic class I CO maturation failure downstream of CO interference patterning in addition to variable fractions of randomly distributed class II COs. In this simulation, class I COs that fail to mature are still sensitive to, and still generate, localised regions of interference, but are removed from the final observed pattern of visible events. In such instances, additional COs are simulated until the final observed simulated frequency matches the frequency observed in experimental datasets. COs arising within 1.5 kb of one another are merged into a single event, again matching the way experimental datasets are processed. **b-g,** Coloured heat maps of P values (KS test) between observed and simulated CO distributions expressed as eCDF curves for the indicated strains. P values >0.9 indicate good statistical fits. Each pixel represents a particular combination of parameter values: maturation failure rate (Y axis) and class II CO % (X axis). See main text and Methods for more details.

FIGURE 5

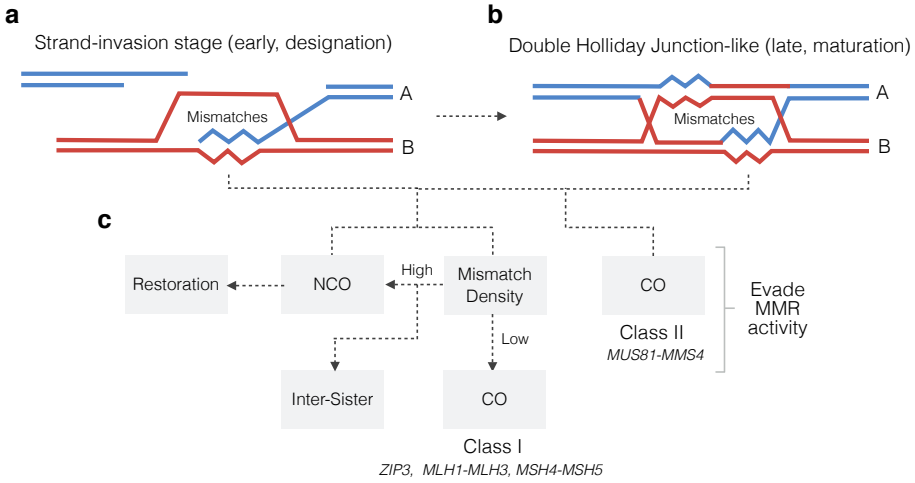

Fig. 6 | Model summarising mismatch-directed suppression of class I COs

a-b, Mismatches (jagged lines) may arise within recombination intermediates at various stages of the meiotic recombination pathway due to differences in sequence between parental information A (blue) and B (red). **c,** In the presence of a functional MMR pathway, regions of higher sequence divergence are proposed to give rise to transient heteroduplexes that cause Msh2-dependent redirection of repair toward the NCO or inter-sister outcomes. Formation of NCOs could arise via destabilisation of nascent strand-invasion intermediates, dissolution of dHJs via Sgs1-Rmi1-Top3, or disruption of CO-biased dHJ resolution (see text for more details). Concomitant repair of mismatches may additionally render some NCO events invisible, and thereby indistinguishable from inter-sister events, due to restoration of parental markers. Inactivation of MMR alleviates such repression arising within CO precursors, increasing the frequency of class I CO formation and thus the spatial uniformity of relative CO positions. In the absence of pro-class I CO factors such as Zip3, Mlh1-3 and Msh4-5, class II COs can arise, but are less subject to Msh2-dependent destabilisation, perhaps due to intrinsic differences in structure, lifespan, and/or extent of heteroduplex DNA. For example, extended branch migration of Holliday junctions at class I precursors (Marsolier-Kergoat et al 2018) which may stabilise such intermediates (Ahuja et al 2021) could increase the probability of hDNA arising within them, and thereby increase Msh2-dependent redirection towards NCO outcomes.

FIGURE 6

Supplementary Figures

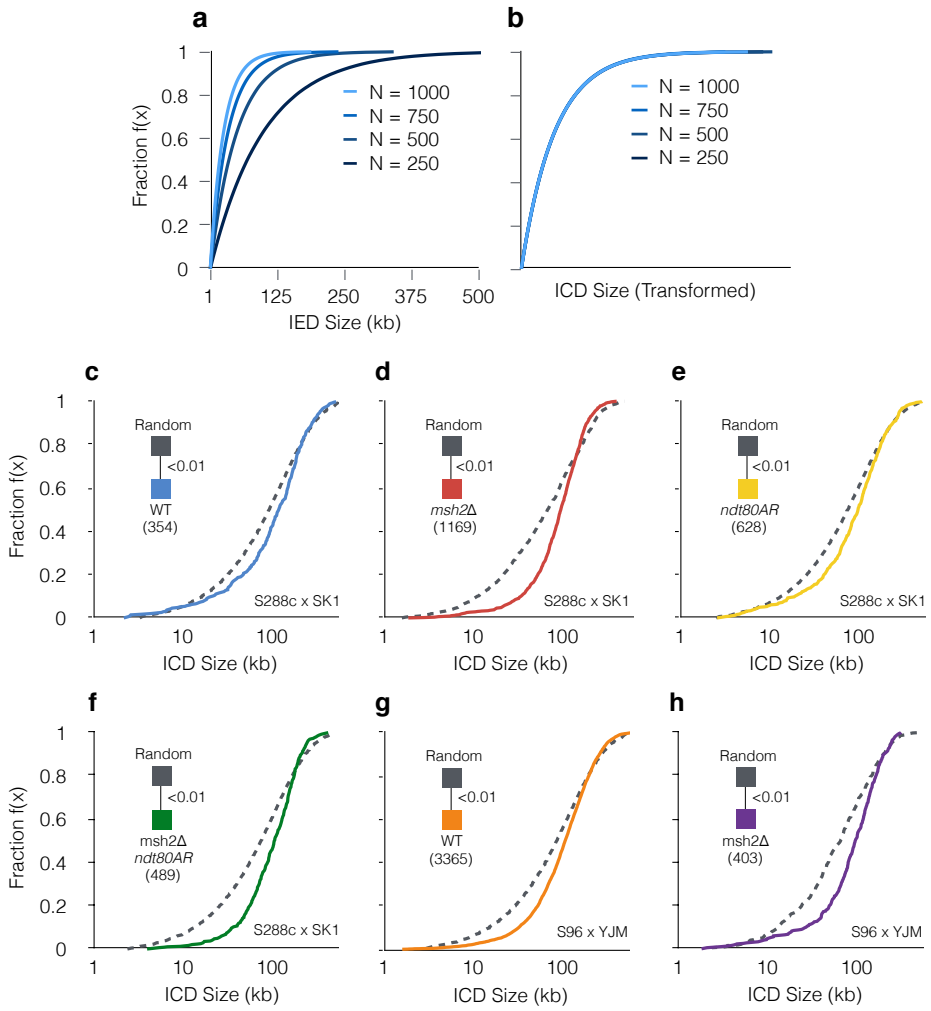

Supplementary Fig. 1 | CO interference is present to varying degrees within all mapped strains

a, Empirical cumulative distribution function (eCDF) showing ICD data derived from interfering simulations (γ(α) = 3.0) at varying CO per cell frequencies (N). **b,** As in **(a)** but ICDs are transformed (see **Methods**) to correct for skews generated by differing CO frequencies. **c-h,** eCDFs showing the fraction of ICDs at or below a given size. The total number of experimental ICDs is indicated in brackets. Randomised datasets were generated via simulation to represent a state of no interference (**Methods**). Pairwise goodness-of-fit tests were performed between genotypes as indicated (triangular legend). P values: Two-sample KS-test.

FIGURE S1

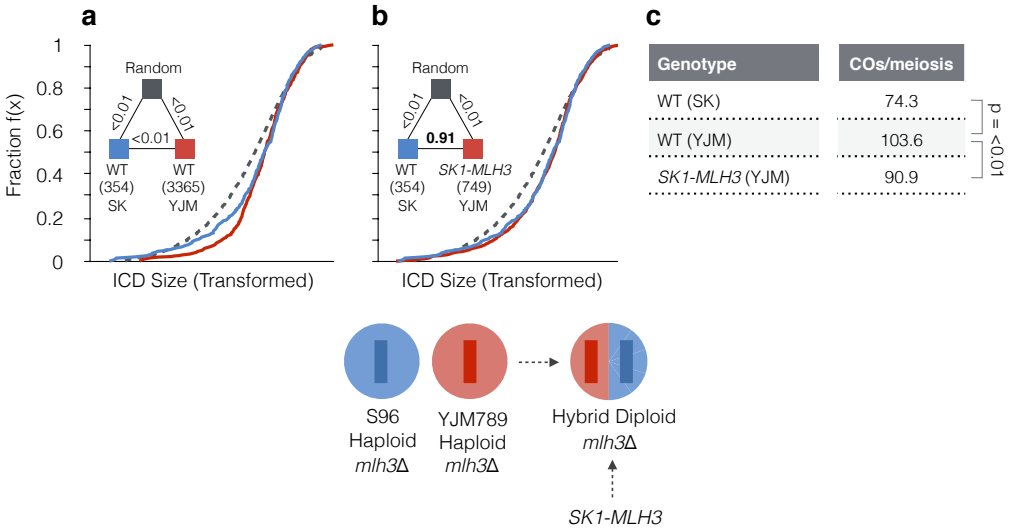

Supplementary Fig. 2 | Cross-specific differences—the *SK1-MLH3* allele has reduced capacity to mediate CO interference

a-b, Empirical cumulative distribution functions (eCDFs) showing the fraction of ICDs at or below a given size. The total number of experimental ICDs is indicated in brackets. ICDs are transformed (see **Methods**) to correct for skews generated by differing CO frequencies. Randomised datasets were generated via simulation to represent a state of no interference (**Methods**). Pairwise goodness-of-fit tests were performed between genotypes as indicated (triangular legend). A schematic of the *SK1-MLH3* strain analysed is shown. P values: Two-sample KS-test. **c,** Average number of COs per meiosis for each genotype. P values: Two-sample T-test.

FIGURE S2

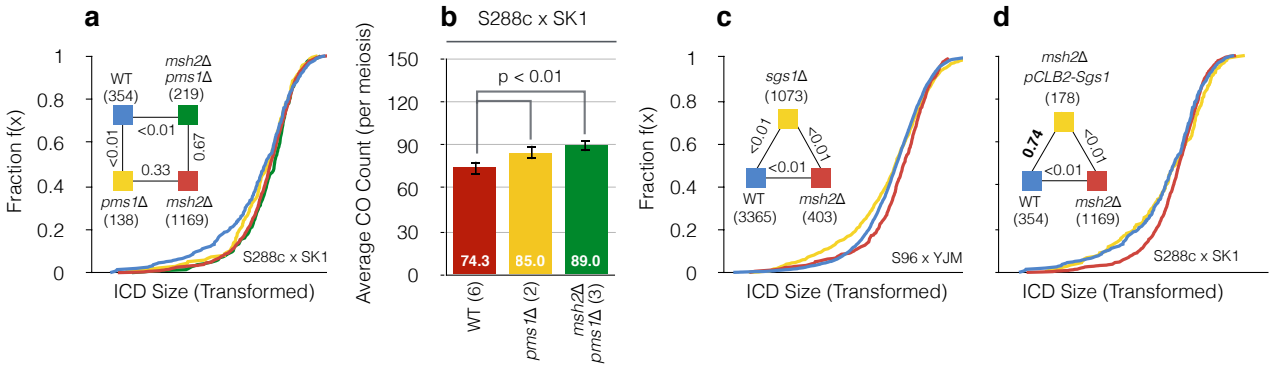

Supplementary Fig. 3 | Mechanistic details of MMR-dependent suppression of interfering COs

a, Empirical cumulative distribution function (eCDF) showing the fraction of ICDs at or below a given size. The total number of experimental ICDs is indicated in brackets. ICDs are transformed (see **Methods**) to correct for skews generated by differing CO frequencies. Randomised datasets were generated via simulation to represent a state of no interference (**Methods**). Pairwise goodness-of-fit tests were performed between genotypes as indicated (triangular legend). P values: Two-sample KS-test. **b,** Average number of COs per meiosis for each genotype. The number of individual meioses sequenced per genotype is indicated. Error bars: 95% confidence intervals (CI*). P values: Two-sample T-test.* **c-d,** As in **(a)** but for differing genotypes.

FIGURE S3

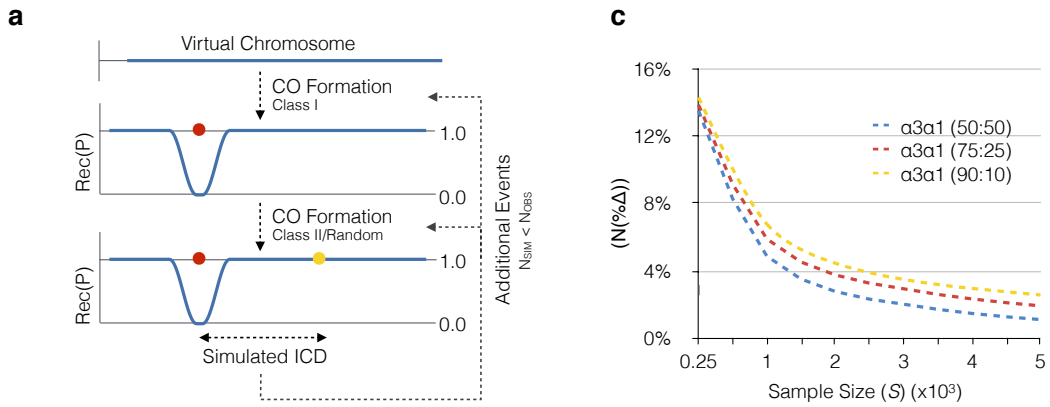

b

		Actual Mixture (Simulated)							Estimated Mixture (γ Mixture Model)						
		S	α1	β1	α2	β2	W_1	W_2	α1	β1	α2	β2	W_1	W_2	N(%Δ)
Variable S		250	3.0	35000	1.0	75000	0.75	0.25	3.45	31139	0.89	84392	0.69	0.31	13.14
		500	3.0	35000	1.0	75000	0.75	0.25	3.29	32889	1.11	69448	0.72	0.28	8.16
		1000	3.0	35000	1.0	75000	0.75	0.25	2.91	35917	0.94	79650	0.78	0.22	5.79
Variable W		1000	3.0	35000	1.0	75000	0.90	0.10	2.83	37110	0.92	78595	0.91	0.09	6.28
		1000	3.0	35000	1.0	75000	0.50	0.50	3.08	36894	0.94	77998	0.48	0.52	4.24
Higher α		1000	4.0	25000	2.0	50000	0.75	0.25	4.09	23976	1.95	51704	0.77	0.23	4.21
		1000	5.0	25000	3.0	50000	0.75	0.25	5.10	25997	3.06	51874	0.78	0.22	4.55

Supplementary Fig. 4 | Modelling CO distributions.

a, *RecombineSim* overview. Virtual chromosomes are constructed at a 100bp resolution as binned, numerical arrays upon which meiotic CO formation is simulated (Methods). Any given 100bp contains a value in the range of [0.0-1.0], designating its recombination potential (Rec(P)). Prior to CO formation, bins are initially populated with [1.0]—denoting an equal probability of class I CO formation in any given bin. During the formation of an interfering CO, *RecombineSim* imposes CO interference as a distance-dependent zone of repression by modifying Rec(P) values according to a hazard function derived from a manually specified γ(α) value, or a γ(α) value estimated from experimental data following gamma (γ) mixture modelling using maximum likelihood expectation (MLE; Methods). Such localised repression around each sequential event thus has the potential to influence the position of all subsequent interfering COs that are simulated. Non-interfering, class II COs are distributed randomly independently of Rec(P) and do not impose, nor are sensitive to, simulated CO interference. Successive events falling within a set threshold of one another (e.g. 1.5 kb) are merged into a single event residing at the midpoint position. These processes repeat until a pre-determined number of simulated ICDs are obtained. **b,** To estimate accuracy of the MLE mixture modelling algorithm, it was used to resolve and estimate individual components of simulated two component mixtures with known parameters (α,β), at known weights (W)—generated via *RecombineSim*. A set of representative examples are shown. Percentage differences between actual and estimated parameters are calculated and averaged to estimate error rate (N(%Δ)) and algorithm accuracy. S = number of ICDs. **c,** Error rate (N(%Δ)) values for three (γ) mixtures calculated at varying sample size (S).

FIGURE S4

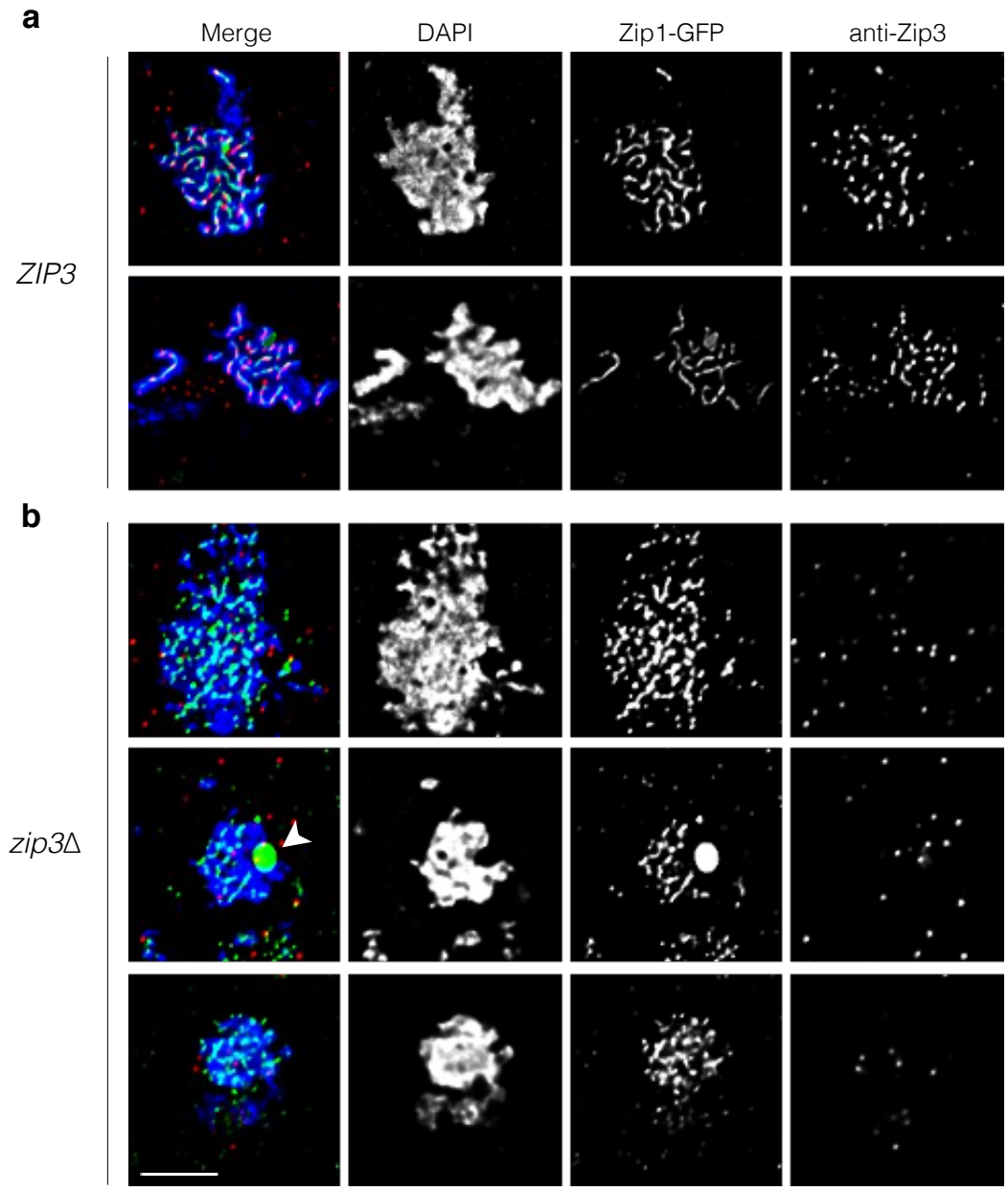

Supplementary Fig. 5 | Specificity of anti-Zip3 antibody

a-b, Representative chromosome spreads of control (**a**) and *zip3*Δ (**b**) cells at the approximate pachytene stage of meiosis, indicated by Zip1-GFP thread-like signals in control cells, but more punctate Zip1-GFP patterns in *zip3*Δ cells (the most complete that they become). Occasional Zip1-GFP polycomplexes were also observed (arrowhead). In *zip3*Δ cells, anti-Zip3 staining detected only background random signals arising from random binding on the slides at locations that were not enriched in the areas of spread chromatin (blue DAPI-stained signals). Scale bar = μm

FIGURE S5

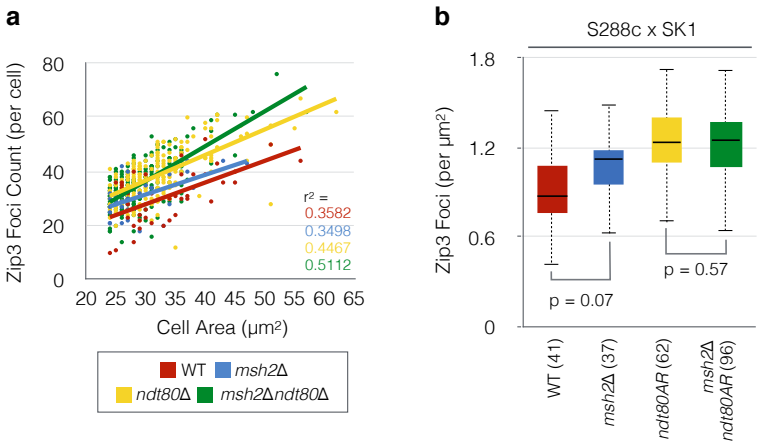

Supplementary Fig 6. Detected Zip3 foci counts are positively correlated with DAPI-delimited nuclear-spread area.

a, Scatter plot of Zip3 foci counts per cell against spread area delimited by the DAPI-positive signal for the indicated strains. R-squared correlation values are shown. **b,** Box-and-whisker plot showing Zip3 foci counts per square micron obtained from chromosome spreads of S288c x SK1 *ndt80*Δ cells prepared at 8 h following induction of meiosis (pachytene arrest). Midlines denote median values, box limits are first and third quartile, whiskers are highest/lowest values within 1.5-fold of interquartile range. P values: Two-sample T-test. The total number of nuclei counted is indicated in brackets.

FIGURE S6

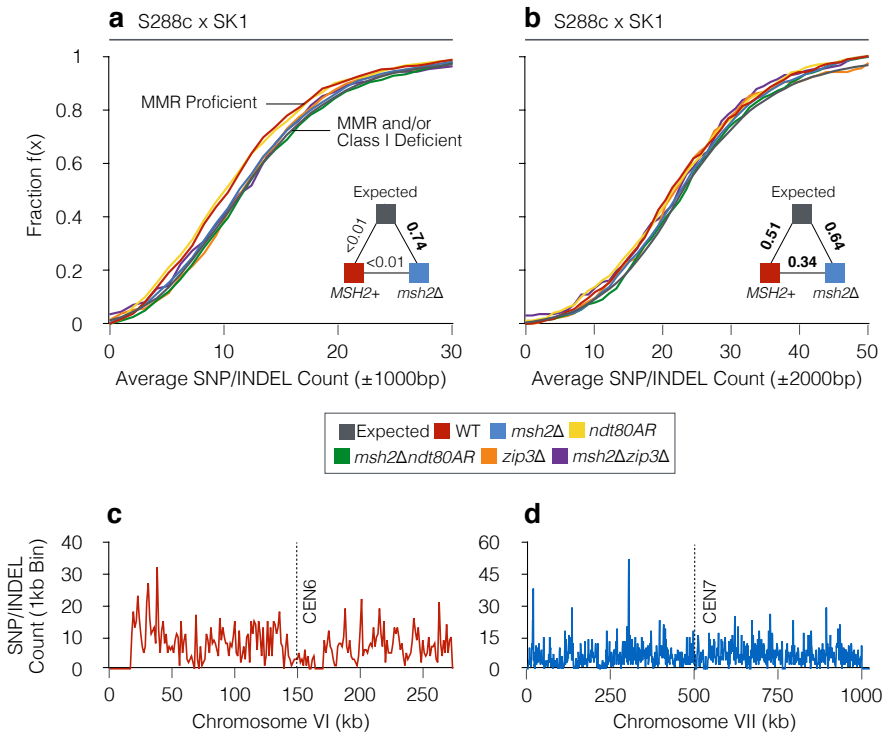

Supplementary Fig. 7 | Localised impact of polymorphism density upon CO formation.

a-b, Empirical cumulative distribution functions (eCDFs) showing the fraction of COs that reside within a region (±1000bp and ±2000bp respectively) of a given SNP/indel count (S288c x SK1 only). Expected is calculated using DSB hotspot midpoints (Pan et al 2011). Pairwise goodness-of-fit tests were performed between pooled *msh2*Δ and *MSH2*+ datasets as indicated (triangular legend). P values: Two-sample KS-test. **c-d,** Example smoothed SNP/INDEL density maps per 1 kb bin in the S288c x SK1 hybrid for ChrVI and ChrVII.

FIGURE S7

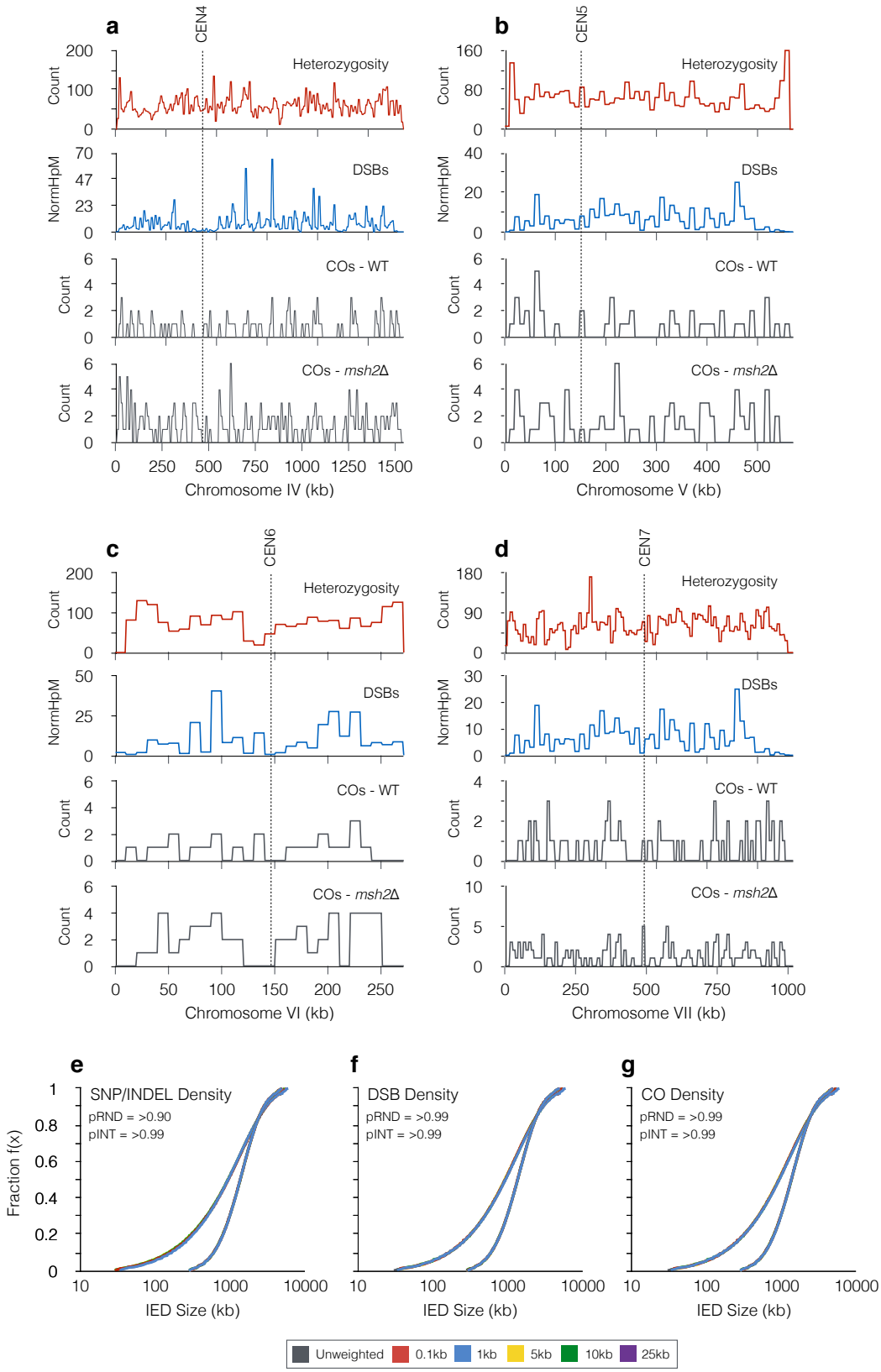

Supplementary Fig. 8 | Impact on simulated CO distributions of local deviations in density of heterozygosity, DSBs, and COs

a-b, Comparison of spatial distribution of population-average densities of heterozygosity, DSB formation (Pan et al. 2011), and CO formation in wild-type and *msh2*Δ cells for four representative chromosomes binned at 10 kb resolution. Although each chromosome has localised deviation from uniformity, each feature is spread relatively evenly across the length of each chromosome. **e-g,** To test the impact that localised deviations in heterozygosity (**e**), DSB formation (**f**), and observed CO density (**g**) might have on relative distributions of COs, simulations of example random (RND; alpha=1) and interfering (INT; alpha=3) gamma distributions were performed as in **Supplementary Fig. 4**, but additionally weighting CO site selection by the relative amplitude of each parameter at varying levels of smoothing (0.1–25 kb). No change in distributions were observed indicating that the nonuniform distribution of these features is unable to significantly bias relative patterns of CO formation. P values reported are the minimum observed out of the five smoothing values tested for each parameter.

FIGURE S8

Relevant genotype	Hybrid	Meioses analysed	Total COs	Total NCOs	COs per meiosis	NCOs per meiosis	ICDs	Source
Wild type	SK1 x S288c	6	446	185	74.3	30.8	354	Crawford et al 2019; This study
*msh2*Δ	SK1 x S288c	13	1377	1206	105.9	92.8	1169	Crawford et al 2019; This study
ndt80AR	SK1 x S288c	8	756	391	94.5	48.9	628	Crawford et al 2019; This study
*ndt80AR msh2*Δ	SK1 x S288c	6	585	521	97.5	86.8	489	Crawford et al 2019; This study
*zip3*Δ	SK1 x S288c	4	187	344	46.8	86.0	153	Crawford et al 2019; This study
*msh2*Δ *zip3*Δ	SK1 x S288c	4	104	1356	26.0	339.0	75	Crawford et al 2019; This study
pms1Δ	SK1 x S288c	2	170	234	85.0	117.0	138	Marsolier-Kergoat et al. 2018
*pms1*Δ *msh2*Δ	SK1 x S288c	3	267	236	89.0	78.7	219	Marsolier-Kergoat et al. 2018
P_{CLB2}*sgs1 msh2*Δ	SK1 x S288c	2	219	183	109.5	91.5	178	Marsolier-Kergoat et al. 2018
Wild type	S96 x YJM789	5	502	261	100.4	52.2	422	Chen et al 2008
Wild type	S96 x YJM789	46	4161	2128	90.5	46.3	3425	Steinmetz
Pooled wild type	S96 x YJM789	51	4663	2389	91.4	46.8	3365	
*msh2*Δ	S96 x YJM789	4	467	225	116.8	56.3	403	Oke et al 2014
*msh4*Δ	S96 x YJM789	6	214	341	35.7	56.8	118	Oke et al 2014
*zip3*Δ	S96 x YJM789	7	429	852	61.3	121.7	317	Oke et al 2014
*mms4*Δ *msh2*Δ	S96 x YJM789	4	391	317	97.8	79.3	327	Oke et al 2014
P_{CLB2}*mms4*	S96 x YJM789	3	321	260	107.0	86.7	273	Oke et al 2014
*mms4*Δ	S96 x YJM789	4	406	321	101.5	80.3	342	Oke et al 2014
Pooled *mms4*	S96 x YJM789	7	727	581	103.9	83.0	616	
*sgs1*Δ	S96 x YJM789	11	1249	848	113.5	77.1	1073	Oke et al 2014
SK1-MLH3	S96 x YJM789	10	909	634	90.9	63.4	749	Al-Sweel et al 2017

Supplementary Table 1 | Summary of whole-genome recombination data analysed in this study.

Meioses analysed indicate the number of four-spore viable tetrads (or eight-spore viable octads for *msh2*Δ SK1 x S288c derivative strains) analysed. Spore viabilities for the SK1 x S288c strains used in this study (as from Crawford et al 2019) are as follows: Wild type 82.0%, *msh2*Δ 73.0, *ndt80AR* 70.4%, *msh2*Δ *ndt80AR* 73.2%, *zip3*Δ 46.2%, *msh2*Δ *zip3*Δ 35.9%. Other samples analyses employ previously published datasets as indicated by Source column. COs and NCOs are total numbers analysed across all meioses of each genotype, or the average number observed per meiosis. ICDs indicates the total number of inter-crossover distances used to assess CO distributions per genotype. For S96xYJM789 two sources of wild-type data were pooled, as were P_{CLB2}*mms4* and *mms4*Δ.

Genotype	Strain	Background	Mat	Genotype
wild type	MJ513	SK1	a	*ho::LYS2 lys2Δ leu2Δ arg4Δ*
	MJ600	S288c	α	*ade8Δ*
msh2Δ	MC26	SK1	α	*ho::LYS2 lys2Δ ura3Δ arg4 leu2 msh2Δ::Kan*
	MC49	S288c	a	*ade8Δ msh2Δ::KanMX*
ndt80AR	MJ43	SK1	α	*ho::LYS2 lys2Δ arg4Δ leu2Δ::hisG trp1Δ::hisG his4XΔ::LEU2 nuc1Δ::LEU2 PGAL1-NDT80::TRP1 ura3::pGPD1-GAL4(848)-ER::URA3*
	MC42	S288c	a	*ade8Δ ndt80Δ::KanMX*
msh2Δndt80AR	MC298	SK1	a	*ho::LYS2 lys2Δ ura3Δ arg4 leu2 trp1Δ::hisG ura3Δ::PGPD1-GAL4(848)-ER::URA3 PGAL1-NDT80::TRP1 msh2Δ::Kan*
	MC300	S288c	α	*ade8Δ ndt80Δ::KanMX msh2Δ::KanMX*
zip3Δ	MC322	SK1	α	*ho::LYS2 lys2Δ ura3Δ arg4 leu2 zip3Δ::HphMX4*
	MC313	S288c	a	*ade8Δ zip3Δ::HphMX4*
msh2Δzip3Δ	MC326	SK1	α	*ho::LYS2 lys2Δ ura3Δ arg4 leu2 msh2Δ::Kan zip3Δ::HphMX4*
	MC317	S288c	a	*ade8Δ msh2Δ::Kan zip3Δ::HphMX4*
Wild type	hLH117	SK1	a	*ho::hisG, lys2, leu2::hisG, trp1::hisG, his3::hisG, ura3, ZIP1-GFP(at AA700)*
	hLH2	S288c	α	*ade8*
msh2Δ	hLH123	SK1	α	*ho::hisG lys2, leu2::hisG, trp1::hisG, his3::hisG, ura3, ZIP1-GFP(at AA700), msh2::KanMX*
	MC49	S288c	a	*ade8 msh2Δ::KanMX*
ndt80AR	hLH127	SK1	α	*ho::hisG, lys2, leu2::hisG, trp1::hisG, his3::hisG, ZIP1-GFP(at AA700), ura3::pGPD1GAL4(848)-ER::URA3, pGAL-NDT80::TRP1*
	MC42	S288c	a	*ade8Δ ndt80Δ::KanMX*
msh2Δndt80AR	hLH130	SK1	a	*ho::LYS2, lys2, leu2::hisG, trp1::hisG, his3::hisG, ZIP1-GFP(at AA700), msh2::KanMX, ura3::pGPD1GAL4(848)-ER::URA3, pGAL-NDT80::TRP1*
	MC300	S288c	α	*ade8Δ ndt80Δ::KanMX msh2Δ::KanMX*

Supplementary Table 2 | Strain Table (S288c x SK1)

TABLE S2